Monthly Notices of the ROYAL ASTRONOMICAL SOCIETY

MNRAS **540,** 3827–3849 (2025)
Advance Access publication 2025 June 14

https://doi.org/10.1093/mnras/staf956

The Compton-thick AGN population and the $N_{\rm H}$ distribution of low-mass AGN in our cosmic backyard

A. Annuar,[1★] D. M. Alexander,[2] P. Gandhi,[3] G. B. Lansbury,[4] M. N. Rosli,[1] D. Stern,[5] D. Asmus,[6] D. R. Ballantyne,[7] M. Baloković,[8,9] F. E. Bauer,[10,11,12] P. G. Boorman,[13] W.N. Brandt,[14,15,16] M. Brightman,[13] C.T.J. Chen,[17,18] A. Del Moro,[19] D. Farrah,[20,21] F. A. Harrison,[13] M. J. Koss,[22] L. Lanz,[23] S. Marchesi,[24,25,26] P. Mohanadas,[1] E. Nardini,[27] C. Ricci[28,29] and L. Zappacosta[30]

Affiliations are listed at the end of the paper

Accepted 2025 June 5. Received 2025 June 3; in original form 2024 December 20

ABSTRACT

We present a census of the Compton-thick (CT) active galactic nucleus (AGN) population and the column density ($N_{\rm H}$) distribution of AGN in our cosmic backyard using a mid-infrared selected AGN sample within 15 Mpc. The column densities are measured from broad-band X-ray spectral analysis, mainly using data from *Chandra* and *NuSTAR*. Our sample probes AGN with intrinsic 2–10 keV luminosities of $L_{2-10,\rm int} = 10^{37}$-$10^{43}$ erg s^{-1}, reaching a parameter space inaccessible to more distant samples. We directly measure a 32^{+30}_{-18} per cent CT AGN fraction and obtain an $N_{\rm H}$ distribution that agrees with that inferred by the *Swift*-BAT survey. Restricting the sample to the largely unexplored domain of low-luminosity AGN with $L_{2-10,\rm int} \leq 10^{42}$ erg s^{-1}, we found a CT fraction of 19^{+30}_{-14} per cent, consistent with those observed at higher luminosities. Comparing the host-galaxy properties between the two samples, we find consistent star formation rates, though the majority of our galaxy have lower stellar masses (by ≈ 0.3 dex). In contrast, the two samples have very different black hole mass ($M_{\rm BH}$) distributions, with our sample having $\approx$1.5 dex lower mean mass ($M_{\rm BH} \sim 10^6$ M$_\odot$). Additionally, our sample contains a significantly higher number of LINERs and HII-type nuclei. The Eddington ratio range probed by our sample, however, is the same as *Swift*-BAT, although the latter dominates at higher accretion rates, and our sample is more evenly distributed. The majority of our sample with $\lambda_{\rm Edd} \geq 10^{-3}$ tend to be CT, while those with $\lambda_{\rm Edd} < 10^{-3}$ are mostly unobscured or mildly obscured.

Key words: techniques: spectroscopic – galaxies: active – galaxies: nuclei – X-rays: galaxies.

1 INTRODUCTION

Many studies have shown that obscured active galactic nuclei (AGNs) dominate the accretion energy budget of the cosmos. This has been evident from the spectral shape of the cosmic X-ray background (CXB) radiation for over three decades (e.g. Setti & Woltjer 1989; Gilli, Comastri & Hasinger 2007; Ueda et al. 2014; Comastri et al. 2015). The obscured phase of AGN accretion is often considered to be a part of an AGN evolutionary scenario in which the central supermassive black hole (SMBH) grows rapidly due to the large amount of gas being driven to the centre of the galaxy as a result of major galaxy mergers (e.g. Martínez-Sansigre et al. 2005; Hopkins et al. 2008; Draper & Ballantyne 2010; Treister et al. 2010; Treister & Urry 2012; Kocevski et al. 2015; Ricci et al. 2017b). This obscured phase is mostly hidden due to enshrouding gas and dust, and is primarily characterized by significant X-ray obscuration. Once the radiation pressure (or winds) from the AGN expels this material, the central source is revealed (Feruglio et al. 2010; Tombesi et al. 2015; Ishibashi & Fabian 2016). However, this scenario might be more relevant at high redshifts.

At lower redshifts such as in the local Universe, the classical AGN unification model (Antonucci 1993; Urry & Padovani 1995) is more likely to be accurate. Based on this model, obscuration is attributed to a dusty, geometrically thick structure, commonly referred to as the 'torus', which surrounds the central SMBH and its accretion disc, obscuring our line-of-sight toward the AGN central region depending on our the viewing angle. Having a complete census of the AGN population over a broad range of obscuration, luminosities, and redshifts is therefore important to help us understand the growth of SMBHs.

To date, however, our understanding of the AGN distribution as a function of the obscuring column density ($N_{\rm H}$) remains highly uncertain, even in the nearby Universe, particularly at the higher end of the distribution; i.e. the Compton-thick (CT) regime ($N_{\rm H} \gtrsim 1.50 \times 10^{24}$ cm^{-2}). As a result of extreme absorption suffered by the nuclear source, direct X-ray emission from CT AGN is significantly suppressed, and the emission that we observe at $\lesssim 10$ keV is often dominated by X-ray photons being scattered or reflected from the back-side of the torus or other circumnuclear material. This observed emission from CT AGN is typically about two orders of magnitude lower than the intrinsic AGN photons emitted in the 2–10 keV band (e.g. Matt et al. 1997; Baloković et al. 2014; Annuar et al. 2017). In extreme cases where the column density exceeds 10^{25} cm^{-2}, the

★ E-mail: adlyka@ukm.edu.my

direct emission from the AGN is severely absorbed over the entire range of X-ray energy, even at the hard X-ray regime ($E > 10$ keV; Gilli et al. 2007). These effects make CT AGN very challenging to identify.

Nevertheless, the CT AGN population is believed to constitute a significant fraction of the entire AGN population. For example, synthesis models of the CXB spectrum suggest that CT AGN are required to produce the CXB radiation and contribute up to 50 per cent of the flux at the peak energy, $E \sim 30$ keV (e.g. Ananna et al. 2019 Gilli et al. 2007; Treister, Urry & Virani 2009 Draper & Ballantyne 2010; Akylas et al. 2012; Ueda et al. 2014; Comastri et al. 2015). Multiwavelength studies of nearby AGN also predict that CT AGN should be numerous, accounting for ~ 30 per cent of the AGN population (e.g. Risaliti, Maiolino & Salvati 1999; Goulding et al. 2011), in agreement with predictions from CXB modelling. Interestingly, of the three AGN identified within $D = 4$ Mpc (Circinus, NGC 4945, and NGC 5128), two are found to be CT (Circinus and NGC 4945), corresponding to a CT AGN fraction of ~ 67 per cent (Matt et al. 2000). Yet, at larger volumes, their census seems to be far from complete. To date, only ~ 8 per cent of AGN out to $z \lesssim 0.055$ have been *directly* identified as CT on the basis of hard X-ray studies by the *Neil Gehrels Swift* Burst Alert Telescope (*Swift*-BAT) survey (Ricci et al. 2015). This is confirmed by the *Nuclear Spectroscopic Telescope Array* (*NuSTAR*; Harrison et al. 2013) study of *Swift*-BAT AGN that measured the same fraction within similar volume (Torres-Albà et al. 2021). These studies suggest that we could be missing a significant number of CT AGN, even in the local Universe. A complete understanding of their population is important to help us accurately characterize the CXB radiation.

In order to form a complete census of the CT AGN population, we first need a complete AGN sample that is least limited by flux and unbiased against obscuration. A volume-limited selection within a relatively small volume is the best approach to construct an AGN sample that is least affected by flux limitations. This means that the sample will include more low-luminosity sources as compared to a purely flux-limited sample. In addition, a volume-limited sample can also be used to form representative volume-averaged statistics.

AGN identification methods at different wavelengths each have their own advantages and disadvantages. For example, AGN selected on the basis of X-ray emission (e.g. an X-ray luminosity threshold) produces a cleaner sample as it suffers relatively lower contamination by the host-galaxy (see Brandt & Alexander 2015; Hickox & Alexander 2018 for reviews). However, such a sample is prone to be biased against finding AGN that are CT, due to extreme X-ray attenuation caused by the high column density of gas and dust. Although optical selection on the basis of emission-line diagnostics (e.g. Baldwin, Phillips & Terlevich 1981; Ho, Filippenko & Sargent 1997; Kewley et al. 2001) is not affected by obscuration by the AGN torus, it can miss AGN that are significantly obscured by the host-galaxy (e.g. Goulding & Alexander 2009). Conversely, an infrared (IR) AGN selection will be relatively unbiased against obscuration due to the lower extinction suffered at this waveband (e.g. the extinction at 12μm is $\sim 27\times$ lower than that in the optical V-band for a standard dust extinction law; Li & Draine 2001). Therefore, it should be the best approach for constructing an AGN sample that is least affected by both host-galaxy and torus obscuration. However, this technique can miss AGN that are severely contaminated by host-galaxy processes such as star formation activity (e.g. Assef et al. 2013; Kirkpatrick et al. 2013).

A multiwavelength selection approach would of course be the best technique to yield the most complete AGN sample that is independent of AGN diagnostics at any one wavelength. However, the advantage of forming a sample using a single waveband selection is that the selection effect is simpler and better understood. Therefore in this paper, we use a sample of local, mid-IR selected AGN within $D \leq 15$ Mpc to form a census of the CT AGN population and the $N_{\rm H}$ distribution of AGN in our cosmic backyard. The $N_{\rm H}$ values and intrinsic luminosities for each AGN were directly measured via broad-band X-ray spectroscopy. In most cases, we used data from multiple focusing X-ray observatories, primarily *Chandra* in combination with the *Nuclear Spectroscopic Telescope Array* (*NuSTAR*; Harrison et al. 2013). We describe our AGN sample in Section 2. In Section 3, we detail the X-ray observations and analysis, including data that were specifically obtained for this programme. The multiwavelength properties of the AGN are discussed in Section 4 to complement our X-ray results. The CT AGN fraction and $N_{\rm H}$ distribution of our sample are presented in Section 5. This is followed by a discussion of the AGN Eddington ratio and host-galaxy properties in comparison with the Swift-BAT AGN sample, in Section 6. Finally, we summarize our results in Section 7.

2 THE $D \leq 15$ MPC AGN SAMPLE

The parent AGN sample that we use for this work was constructed by Goulding & Alexander (2009) (hereafter GA09; see also Goulding et al. 2010). Here, we briefly describe their AGN selection, and refer the reader to GA09 and its subsequent paper, Goulding et al. (2010), for further details on the sample. Their sample consists of 17 IR-selected AGN within $D = 15$ Mpc. It was derived using the *Infrared Astronomical Satellite* (*IRAS*) Revised Bright Galaxy Sample (RBGS; Sanders et al. 2003) which provides the most complete census of IR-bright galaxies ($f_{60\,\mu\rm m} > 5.24$ Jy) in the local Universe above a Galactic latitude of $|b| = 5^{\circ}$. The constraint of 15 Mpc on the distance was placed to avoid the Virgo cluster at ≈16 Mpc so that the AGN sample is representative of the field-galaxy population, as demonstrated in Goulding et al. (2010). The distances were calculated using the Mould et al. (2000) cosmic attractor model which adjusts heliocentric redshifts to the centroid of the Local Group, taking into account the gravitational attraction toward the Virgo Cluster, the Great Attractor, and the Shapley supercluster. In addition, GA09 apply a total IR (8–1000μm) luminosity cut-off of $L_{\rm IR} > 3 \times 10^9\,{\rm L}_{\odot}$ to their sample to match the flux-sensitivity limit of RBGS, and exclude low-luminosity dwarf galaxies as well as relatively inactive galaxies with low star formation rate. In total, GA09 found that there are 67 galaxies detected by IRAS with $L_{\rm IR} > 3 \times 10^9\,{\rm L}_{\odot}$ within $D \leq 15$ Mpc.[1]

GA09 then used the detection of the high-ionization [Ne V]λ14.3μm emission-line by the *Spitzer Space Telescope* (Werner et al. 2004) high resolution IR Spectrographs (IRS) Short-High (SH) module ($\lambda = 9.9$–19.6μm; spectral resolution $R \sim 600$; aperture size $= 4.7 \times 11.3$ arcsec^2; Houck et al. 2004) to identify the presence of AGN in these galaxies. Out of the 67 galaxies, 64 have *Spitzer*-IRS SH data (~ 94 per cent complete). The [Ne V] line is primarily produced in the NLR of AGN through ionization by the primary emission of the nuclear source. Because the line is produced in the NLR, it is not strongly affected by obscuration by the AGN torus, unlike the primary emission. In addition, given that

[1]GA09 presented 68 galaxies in their sample. However, we find that one of the galaxies; NGC 3486, has an IR luminosity below the threshold value ($L_{\rm IR} = 2.04 \times 10^9\,{\rm L}_{\odot}$). Therefore, we exclude NGC 3486 from the sample in this paper.

it is emitted at mid-IR wavelength (i.e. $\lambda = 14.32$ μm), it does not suffer from significant absorption by the host-galaxy, as opposed the NLR emission-lines that are produced at optical wavelengths (the extinction at 14.32 μm is $\sim 50\times$ lower than that in the optical V-band; Li & Draine 2001). The energy required to ionize this line is also relatively large; i.e. 97.1 eV, meaning that it can only be produced by extremely energetic phenomena such as AGN activity. The detection of this line therefore provides an almost unambiguous identifier of AGN (Weedman et al. 2005; Iwasawa et al. 2011; Negus et al. 2023). Although the line is predicted to be produced by a dense population of Wolf-Rayet stars (Schaerer & Stasińska 1999) and extremely high velocity shocks caused by a starburst, these were not observed by *Spitzer*, and do not appear to be the case for the AGN in the GA09 sample (see GA09 for further details).

Based on this technique, GA09 found 17/64 galaxies (27^{+13}_{-10} per cent) have significant [Ne V] line detections, and thus are identified as AGN.[2] To further extend the GA09 sample, we included two other known AGN within 15 Mpc that match the GA09 selection criteria, but were not originally selected. These are Circinus and NGC 4565. Circinus is identified as an AGN in optical and X-ray data (e.g. Moorwood & Glass 1984; Baumgartner et al. 2013), but was not selected in the original RBGS sample (therefore GA09) due to its low Galactic latitude; i.e. $\sim 4^{o}$ below the Galactic plane (see also Section 2.1). NGC 4565 was one of the galaxies in GA09 that lacked high-resolution *Spitzer*-IRS spectroscopic data at the time of that study but has since been observed with the high-resolution spectrograph. Pereira-Santaella et al. (2010) present the high-resolution *Spitzer*-IRS data for both Circinus and NGC 4565, and detected [Ne V] emission-lines in both galaxies. These galaxies are also identified as Seyferts on the basis of their optical emission-line ratios (Ho et al. 1997) and have [O IV]λ25.89μm line detections (Diamond-Stanic, Rieke & Rigby 2009).[3] Our final sample thus consists of 19 AGN within $D = 15$ Mpc. The complete list of the AGN and their basic properties are presented in Table 1.

Out of these 19 AGN, 8 (42^{+34}_{-21} per cent) are not identified as AGN using the optical emission-line diagnostic diagram (see Table 1) due to significant dilution by the host galaxies (e.g. highly inclined, presence of dust lanes, strong star formation activity; GA09). Furthermore, 10/19 (53^{+37}_{-23} per cent) are found to be unidentified as AGN in X-rays on the basis of high X-ray energy non detection by the *Swift*-BAT 105-month all sky survey (Oh et al. 2018).[4] This demonstrates the relative inefficiency of identifying AGN using optical and X-ray wavelengths as compared to IR spectroscopy (i.e. $\lesssim 50$ per cent in this case).

In addition, only 1/19 ($5.0^{+21}_{-4.8}$ per cent) and 7/19 (37^{+33}_{-20} per cent) of our sources overlapped with the *NuSTAR* Local AGN $N_{\rm H}$ Distribution Survey (NuLANDS; Boorman et al. 2024a) and the Local AGN Survey (LASr; Asmus et al. 2020), respectively, which used infrared colours AGN selection method. This corresponds to inefficiencies of $95^{+5.0}_{-34}$ per cent and 63^{+37}_{-26} per cent, respectively, when using this technique in AGN identification, particularly for those with low luminosity and when the AGN contribute only a small fraction of the total galaxy emission.

2.1 Sample Completeness

In extreme cases where the nuclei of the galaxies are highly obscured such as in merging galaxies and Compact Obscured Nuclei (CONs; eg Sakamoto et al. 2013; Martín et al. 2016; Aalto et al. 2019), even the [Ne V] line can be extinguished and undetected. An example of this is the local prototype of a deeply buried nucleus in NGC 4418 (e.g. Roche et al. 1986; González-Alfonso & Sakamoto 2019; Wethers et al. 2024). This galaxy is located at a distance of 31.9 Mpc (Sanders et al. 2003) and therefore lies beyond of our sample's distance threshold. It is prominent for its unusual deep silicate absorption feature at 9.8 μm (e.g. Rieke & Lebofsky 1985; Roche et al. 1986; Spoon et al. 2007; Stierwalt et al. 2013), indicating extreme extinction. The presence of an AGN has long been suggested by numerous studies based on multiple pieces of evidence (e.g. Roche et al. 1986; Spoon et al. 2001; Sakamoto et al. 2021), including the presence of a warm IR spectral energy distribution (SED), indicating a hidden hot source, likely an AGN accretion disc. However, the [Ne V] emission-line was not detected in the galaxy by *Spitzer* (Spoon et al. 2022), which could be due to the extreme absorption suffered by the nucleus.

We can therefore take NGC 4418 as a model galaxy in order to investigate if GA09 may have missed more AGN within their galaxy sample due to similar cause. Given the distinctive IR properties of NGC 4418, we search for evidence of a warm IR SED and deep silicate absorption. The IRAS $f_{60\mu m}/f_{25\mu m}$ flux ratio can be used as an indicator for a warm IR SED. Galaxies with an AGN would have warmer IRAS colours and therefore smaller $f_{60\mu m}/f_{25\mu m}$ ratios. Fig. 1 (top) shows the distribution of $f_{60\mu m}/f_{25\mu m}$ ratio for the galaxies in GA09, AGN in our sample and NGC 4418. We use a $f_{60\mu m}/f_{25\mu m}$ threshold value of ≤ 5 to indicate AGN-dominated SED based on Alexander (2001), and which is sufficiently 'warm' to include NGC 4418. Based on the figure, we see that only three AGN in our sample (Circinus, NGC 1068, and NGC 4051) are identified using this technique. Interestingly, there are three additional galaxies in the GA09 sample with undetected [Ne V] line emission that falls below our $f_{60\mu m}/f_{25\mu m}$ threshold: IIZW 40, M 82, NGC 4818.

For these three galaxies however, there has been no convincing evidence for AGN in earlier studies. These galaxies also do not have extreme silicate absorption like NGC 4418, which implies that the extinction towards their mid-IR emission is not sufficiently high to detect [Ne V] emission from the central source, if any. In fact, their silicate absorption is comparable to most of the AGN in our sample shown in Fig. 1 (bottom), which means that GA09 should have been able to detect the line if a significant AGN existed in these galaxies. In addition, their 6.2 μm polycyclic aromatic hydrocarbon (PAH) equivalent widths are relatively high and are typical for starburst galaxies (Spoon et al. 2022), except for IIZW 40 which shows a hot-dust dominated spectrum, typical for an AGN on the basis of its silicate strength and PAH feature (Spoon et al. 2022). However, we argue that this system is a metal-poor dwarf galaxy and thus may not follow the same trends and features of more massive galaxies. Because of this and due to the lack of other evidence for the presence

[2]The uncertainties were calculated using the approximate algebraic expression for small number Poisson statistics, based on the 90 per cent confidence double-sided interval (95 per cent single-sided) given in Gehrels (1986), with the upper limit capped at 100 per cent.

[3]The [O IV]λ25.89μm emission-line is also often used for AGN identification due to its high ionization energy (59.4 eV). However, it is a more ambiguous AGN indicator than the [Ne V] line since energetic starbursts can also produce this line.

[4]The *Swift*-BAT telescope provides a hard X-ray all sky survey in the 14–195 keV band. The 105-month survey is sensitive down to an X-ray flux of $f_{14-195,\rm obs} \sim 8 \times 10^{-12}$ erg s^{-1} cm^{-2} (Oh et al. 2018). This means that at $D = 15$ Mpc, it is able to detect an AGN down to an observed X-ray luminosity of $L_{14-195,\rm obs} \sim 2 \times 10^{41}$ erg s^{-1}, or $L_{2-10,\rm obs} \sim 8 \times 10^{40}$ erg s^{-1} on the basis of the scaling relation derived by Rigby, Diamond-Stanic & Aniano (2009).

Table 1. Complete list of AGN at $D \leq 15$ Mpc and their basic properties.

Name	D	Hubble	Spectral	*Swift-BAT*	log M_{BH}	log $L_{[OIV]}$	log $L_{[NeV]}$	log $L_{12\mu m}$	log $L_{[OIII],corr}$	log L_{IR}	*NuSTAR*
	[Mpc]	Type	Class	AGN?	[$M_\odot$]	[erg s^{-1}]	[erg s^{-1}]	[erg s^{-1}]	[erg s^{-1}]	[$L_\odot$]	obs.?
(1)	(2)	(3)	(4)	(5)	(6)	(7)	(8)	(9)	(10)	(11)	(12)
Circinus	4.0	Sb	S2	Yes	6.23[2]	40.11[4]	39.62[5]	42.60	40.52[8]	10.15[10,11]	Yes
ESO121-G6	14.5	Sc	H II	No	6.10	39.04	38.21	40.28[6]	-	9.70	Yes*
NGC 0613	15.0	Sbc	H II	No	7.34	39.38	38.25	41.27	39.67	10.37	No
NGC 0660	12.3	Sa	L	No	7.35	39.71	38.85	41.18[6]	40.03	10.49	Yes*
NGC 1068	13.7	Sb	S2	Yes	7.20	41.66	41.30	43.76	42.61	11.27	Yes
NGC 1448	11.5	Scd	S2[1]	No	5.99	39.40	38.76	40.60[1]	38.84[1]	9.78	Yes*
NGC 1792	12.5	Sbc	H II	No	6.83	38.26	37.88	< 42.03[7]	-	10.33	Yes*
NGC 3621	6.6	Sd	S2	No	6.50	38.18	37.18	< 40.75[7]	37.19	9.74	Yes*
NGC 3627	10.0	Sb	L	No	7.30	38.38	37.55	40.59	39.01	10.38	Yes*
NGC 3628	10.0	Sb	L	No	6.53	38.81	38.05	< 40.47	36.97	10.25	Yes*
NGC 4051	13.1	Sbc	S1	Yes	6.15	39.88	39.36	42.38	40.25	9.90	Yes
NGC 4565	10.0	Sb	S2	No	7.56[3]	38.40	37.58[5]	< 41.35[7]	38.84[9]	9.66	No
NGC 4945	3.9	Scd	S2	Yes	6.04	38.72	38.11	40.00	35.04	10.48	Yes
NGC 5033	13.8	Sc	S1	Yes	7.62	39.08	37.98	40.96	39.78	10.13	Yes
NGC 5128	4.0	S0	H II	Yes	8.38	39.38	38.62	41.86	38.09	10.11	Yes
NGC 5194	8.6	Sbc	S2	Yes	6.88	38.85	37.81	40.80	40.18	10.42	Yes
NGC 5195	8.3	Irr	L	No	7.31	37.89	37.22	< 41.90[7]	37.12	9.50	Yes
NGC 5643	13.9	Sc	S2	Yes	6.44	40.43	39.75	42.17	41.32	10.24	Yes*
NGC 6300	13.1	Sb	S2	Yes	6.80	39.78	39.41	42.45	40.02	10.09	Yes

Notes. Column (1) Galaxy name; (2) Distance in Mpc; (3) Hubble classification of the host-galaxy; (4) Optical spectral class on the basis of emission-line diagnostic diagrams (Kewley et al. 2001; Kauffmann et al. 2003); (5) Whether the AGN is detected in the 105-month *Swift*-BAT survey (Oh et al. 2018); (6) Logarithm of the black hole mass relative to the mass of the Sun, $M_\odot$ measured from various techniques (e.g. maser mapping, velocity dispersion, and bulge luminosity; see GA09 for more details); (7)−(10) [O IV], [Ne V], 12 μm continuum, and [O III] (corrected for the Balmer decrement) luminosities in logarithmic scale and expressed in erg s^{-1}, respectively; (11) Logarithm of the total IR luminosity in solar luminosities, $L_\odot$; (12) Whether the AGN has been observed by *NuSTAR*. Most data are taken from GA09 or Goulding et al. (2010), unless indicated otherwise. The spectral classes for the *Swift*-BAT detected AGN were obtained from Oh et al. (2022).

* observed as part of our programme. *References.* [1] Annuar et al. (2017); [2] Greenhill et al. (2003); [3] McKernan, Ford & Reynolds (2010); [4] Diamond-Stanic et al. (2009); [5] Pereira-Santaella et al. (2010); [6] Annuar et al. (2020); [7]*WISE* 12μm luminosity used as upper limit [8] Bianchi et al. (2002); [9] Ho et al. (1997); [10] Helou & Walker (1988); [11] Sanders & Mirabel (1996).

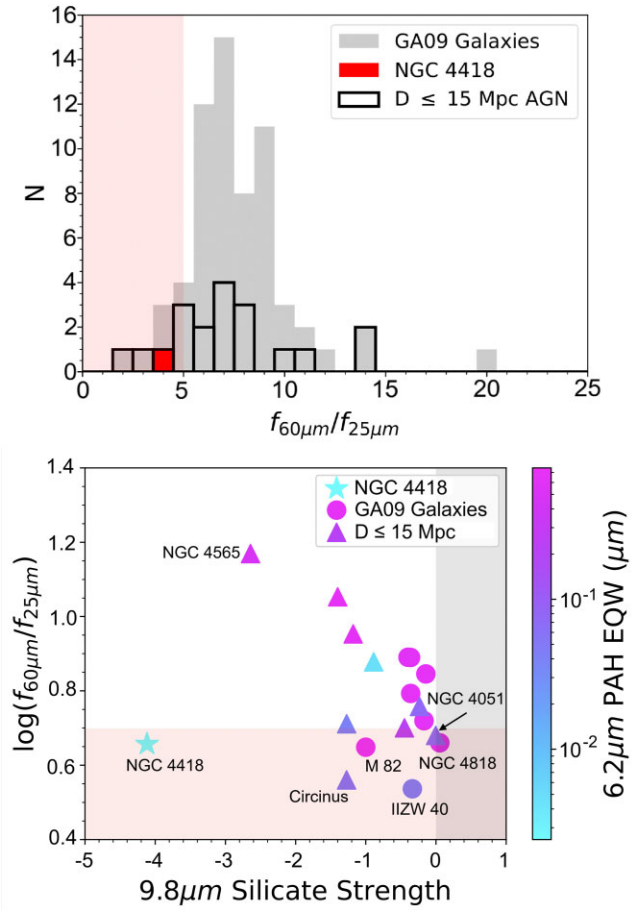

Figure 1. *Top*: Distribution of IRAS $f_{60\,\mu m}/f_{25\,\mu m}$ ratio for the galaxies in GA09 (grey), our AGN sample (black solid line), and NGC 4418 (red). The pink shaded region marks a flux ratio of ≤ 5, indicating an AGN-dominated SED. *Bottom*: IRAS $f_{60\,\mu m}/f_{25\,\mu m}$ versus 9.8 μm silicate strength for GA09 galaxies (circles), our AGN sample (triangles), and NGC 4418 (star); silicate and 6.2 μm PAH equivalent-width measurements are taken from Spoon et al. (2022). Marker colours denote different PAH equivalent-width strengths (a star-formation indicator). The pink region marks $f_{60\,\mu m}/f_{25\,\mu m} \leq 5$ (AGN-dominated spectra); the grey region marks silicate emission instead of absorption.

of AGN in the galaxy (Leitherer et al. 2018), we therefore infer that it does not host an AGN.

Based on the *Swift*-BAT 105-month survey (Oh et al. 2022), there are five additional AGN that are detected which lies within our distance threshold and not selected in GA09, and therefore our sample (see Fig. 2). They are M81, M106, NGC 1566, NGC 4151, and NGC 4395. However, only three of these are found to be located within 15 Mpc if we were to use the same distance calculation method by Mould et al. (2000) as in GA09. These are M81, M106, and NGC 4395. NGC 4395 is a dwarf galaxy with $f_{60\,\mu m} < 5.24$ Jy, and therefore was excluded in the RBGS sample (Sanders et al. 2003). M81 has an IR luminosity of $L_{IR} = 2.95 \times 10^9\,L_\odot$ (Sanders et al. 2003), which is just below GA09 selection criteria. M106 is not in the RBGS sample, although it would have matched all the galaxy selection criteria in GA09. However, *Spitzer* did not detect [Ne V] emission from the galaxy (Spoon et al. 2022).

Finally, based on the *Swift*-BAT survey, Circinus is the only AGN that is found within the Galactic latitude. Based on all these, we deduce that GA09 did not clearly miss any AGN in their galaxy

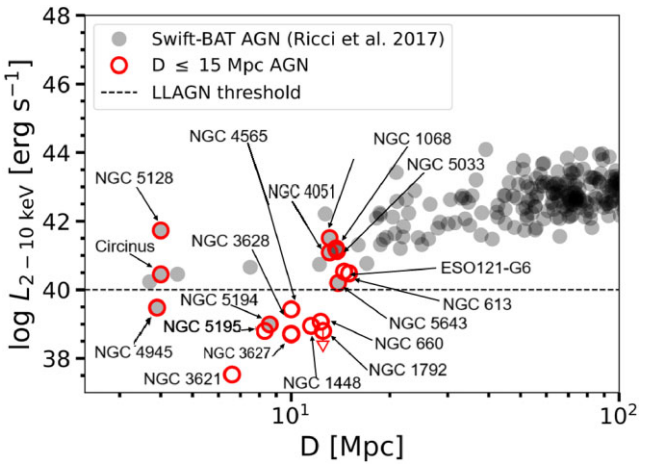

Figure 2. 2–10 keV luminosity versus distance for the AGN in our sample (observed luminosity; red), in comparison with the *Swift*-BAT AGN detected in the 70-month survey (intrinsic luminosity; grey; Ricci et al. 2015). Our AGN sample extends approximately two orders of magnitude beyond the fainter end of the *Swift*-BAT AGN sample (dashed line). *Swift*-BAT AGN within 15 Mpc that are not in our sample are discussed in Section 2.1.

sample on the basis of their selection criteria. Hence, we conclude that our AGN sample can be assumed to be near complete.

3 X-RAY OBSERVATIONS AND DATA REDUCTION

Throughout our studies on the $D < 15$ Mpc sample, *Chandra* data is critical as it provides us with high resolution X-ray images of the galaxies which is important in isolating the AGN emission from off-nuclear sources and accounting for contaminants in the AGN emission in data obtained by other telescopes (e.g. Annuar et al. 2017, 2020). This is especially crucial for our AGN sample where about half of our sources have very low observed X-ray luminosities; i.e. $L_{2-10,obs} \leq 10^{39}$ erg s^{-1} (see Fig. 2), comparable to ultraluminous X-ray sources. This makes them prone to significant contamination by host-galaxy emission. Sensitive high-energy X-ray data from *NuSTAR* have also been demonstrated to be important to provide good quality high-energy data for these low-luminosity sources which are not detected by *Swift*-BAT. Broadband X-ray data are essential for characterizing the AGN spectra accurately in order to obtain reliable measurements of their properties.

Among the 19 AGN, broad-band X-ray spectral analyses for 13 sources ($\sim$ 68 per cent) have been performed in detail by past studies utilizing low-energy data from *Chandra* and/or *XMM-Newton*, and high-energy data from *NuSTAR* and/or *Swift*-BAT, mostly using physically motivated torus models by e.g. Murphy et al. (2012), Brightman & Nandra (2008) and/or Baloković et al. (2018), to measure the X-ray properties of the AGN, including their torus column densities and intrinsic luminosities (see Table 3). The analyses for five of these sources were published as part of our work in Annuar et al. (2015, 2017, 2020). To improve the X-ray completeness, we acquired a total of 8 *NuSTAR* observations, of which five were coordinated with *Chandra* (three), *XMM-Newton* (one) or *Swift*-XRT (one). This boosted the *Chandra* and *NuSTAR* data for our sample from $\sim$ 89 per cent to 100 per cent, and $\sim$ 47 per cent to $\sim$ 89 per cent complete, respectively. We did not propose *NuSTAR* observations for the remaining two ($\sim$ 11 per cent) AGN (i.e. NGC 613 and NGC 4565) since we believe that the archival

low-energy X-ray data for those two sources already provide reliable measurements on their column densities and AGN properties (see Table 1).

In this section, we present the X-ray observations and analyses for these remaining six objects in our sample. We note that most of the data for these AGNs have been analysed and published in past papers. However, we re-analysed them here to ensure our analyses are consistent with our previous studies. The X-ray observations used in this paper are detailed in Table 2.

As mentioned earlier, we prioritize low-energy X-ray data from *Chandra* in our analysis. The *Chandra* data were reprocessed to create event files with updated calibration modifications using the CIAO pipeline (Fruscione et al. 2006), following standard procedures. We then used the DMCOPY task to produce X-ray images of each source in different energy bands, and extracted the source spectra using the SPECEXTRACT task in CIAO. One of our sources (NGC 3621) has coordinated *NuSTAR* and *XMM-Newton* observations, which we present in this paper. We analysed the Pipeline Processing System (PPS) data products using the Science Analysis Software (SAS), with standard filter flags. Background flares were subtracted from the data by visually examining the source light curves, and the X-ray spectra from the three EPIC cameras were then extracted using the EVSELECT task in SAS.

In addition to these, we also used high-energy X-ray observations from *NuSTAR* where available to facilitate our X-ray spectral analysis of the AGN at high energies. We processed the *NuSTAR* data for our sources with the *NuSTAR* Data Analysis Software (NUSTARDAS) within HEASOFT. The NUPIPELINE script was used to produce the calibrated and cleaned event files using standard filter flags. We extracted the spectra and response files from each of the *NuSTAR* focal plane modules, named A and B (FPM A and FPM B), using the NUPRODUCTS task. In addition to the spectral extraction, we also combined the *NuSTAR* event files from the two FPMs using XSELECT to produce the total event file. The total image counts at different energy bands were then produced from the resultant event files using the DMCOPY task in CIAO.

In all cases, the spectra and response files from each *NuSTAR* FPM are combined using the ADDASCASPEC script to increase the overall signal-to-noise ratio of the data in our spectral fitting (see Section 4).[5] For *XMM-Newton* data (NGC 3621), spectra extracted for the EPIC MOS1 and MOS2 cameras were combined using the EPICSPECCOMBINE task in SAS. In most cases, we binned our spectra to a minimum of 20 counts per bin to allow the use of χ^2 statistics. However, for cases in which the count rate is relatively low (<200 counts), we grouped the spectra to a minimum of 5 counts per bin for the *NuSTAR* and *XMM-Newton* data, and 1 count per bin for the *Chandra* data, and optimized our fitting using the Poisson C-statistic (Cash 1979). This was done using the GRPPHA task in HEASOFT.

4 X-RAY SPECTRAL ANALYSES

The X-ray spectral analysis was performed using XSPEC. We included a fixed Galactic absorption component for each source (Kalberla et al. 2005) using the XSPEC model 'PHABS' in all spectral fits, and assumed solar abundances for all models. Redshifts for all sources were obtained from the NASA/IPAC Extragalactic Database (NED).

[5]More details on the ADDASCASPEC script can be found at https://heasarc.gsfc.nasa.gov/docs/asca/adspecinfo.html.

Due to the modest quality of most of our data, we also fixed the cross-calibration uncertainties of each observatory with respect to *NuSTAR* to the values found by Madsen et al. (2015) using a constant parameter, C. In general, we started our analysis using a simple absorbed power-law model to provide an initial indication of the level of obscuration suffered by the AGN. If the model indicated that the sources were obscured with $N_{\rm H} \geq 10^{22}$ cm^{-2}, we then utilized the physically motivated torus models by Murphy et al. (2012) (MYTORUS) and Baloković et al. (2018) (BORUS). We did not use these models for the unobscured sources due to the model limitations, which could only measure column densities down to $N_{\rm H} = 10^{22}$ cm^{-2}. In all cases, we used the most simple version of the MYTORUS and BORUS models, with all the AGN emission components tied together and most non-crucial parameters (e.g. torus inclination angle, iron abundance, and high-energy cut-off) fixed to the recommended values. We refer the reader to Murphy et al. (2012), Baloković et al. (2018), and our previous works (Annuar et al. 2015, 2017, 2020) for more detailed information on the modelling technique used. We summarize the main results of our spectral analysis in Table 3. All errors are quoted at 90 per cent confidence. Below we discuss the individual sources and their spectral analysis results.

4.1 NGC 613

NGC 613 is an Sbc galaxy located at a distance of $D = 15$ Mpc. Evidence for the presence of an AGN in the galaxy was provided by GA09 on the basis of [Ne V] emission and the presence of nuclear radio jet (Hummel et al. 1987; Hummel & Jorsater 1992; Miyamoto et al. 2017). Nuclear water maser emission has also been detected in the galaxy (Kondratko et al. 2006). The AGN is unidentified in the optical wavebands (i.e. classified as HII in optical; GA09) and it is not detected in the *Swift*-BAT survey (Oh et al. 2018).

The AGN is surrounded by a starburst ring (Hummel & Jorsater 1992; Falcón-Barroso et al. 2014; Audibert et al. 2019), but using high angular resolution mid-IR observations (∼0.4 arcsec) by Gemini T-ReCS, Asmus et al. (2014) managed to resolve the compact nucleus from this circumnuclear ring. The nuclear region was recently studied in great detail by da Silva et al. (2020a, b) using multiwavelength data in order to understand its complexity. The nucleus has been observed in X-rays by *XMM-Newton* and *Chandra* in 2010 and 2014, respectively. Castangia et al. (2013) analysed the *XMM-Newton* data and measured a column density of $N_{\rm H} = (36.0 \pm 5.0) \times 10^{23}$ cm^{-2}, indicating that it is heavily obscured, but Compton-thin. The *Chandra* data are analysed in da Silva et al. (2020a), though no column density measurement was presented.

4.1.1 X-ray observations and spectral fitting

We re-analyse the *Chandra* data of NGC 613 to obtain the column density value from this higher resolution X-ray observation. We did not try to obtain a *NuSTAR* observation for this object as there were no indications of it being a CT AGN based on multiwavelength diagnostics (see Figs 12 and 13), and thus the current X-ray data are sufficient to provide us with a reliable column density measurement. The AGN is clearly detected in the *Chandra* data, located at RA = 1:34:18.23, Dec. = −29:25:06.35 as determined by the WAVDETECT tool within CIAO in the 2–8 keV energy band. In Fig. 3, we show the combined *Chandra* RGB image of NGC 613. We extracted the spectra of the AGN using an 8 arcsec-radius circular region to incorporate all the source emission. The total net count rate obtained

Table 2. Log of additional X-ray observations used in this work.

Name	R.A.	Dec.	Observatory	ObsID	Date	Energy band	t_{exp}	Extraction Region	Count rate	Previous work
						(keV)	(ks)	(arcsec)(	(10^{-3} cts s^{-1})	
(1)	(2)	(3)	(4)	(5)	(6)	(7)	(8)	(9)	(10)	(11)
NGC 613	1:34:18.23	−29:25:06.35	*Chandra*	16 351	2014-08-21	0.5–8	48.9	8	45.14 ± 0.97	da Silva, Menezes & Steiner (2020a)
NGC 1792	5:05:14.58	−37:58:50.85	*Chandra*	19 524	2016-11-23	0.5–8	19.8	20	6.42 ± 1.22	...
			NuSTAR	60 371 001 002	2018-05-13	3–24	45.7	20	<0.49	...
NGC 3621	11:18:16.51	−32:48:50.78	*Chandra*	9278	2008-03-06	0.5–8	21.2	3	1.06 ± 0.30	Gliozzi et al. (2009)
			XMM-Newton	0 795 660 101	2017-12-16	0.5–10	56.4	30	602 ± 5	...
			NuSTAR	60 371 002 002	2017-12-15	3–24	61.4	30	10.90 ± 0.50	Osorio-Clavijo et al. (2022)
NGC 3627	11:20:15.04	+12:59:29.92	*Chandra*	394	1999-11-03	0.5–8	1.8	2	6.17 ± 1.98	Panessa et al. (2006)
			...	9548	2008-03-31	0.5–8	49.6	2	5.09 ± 0.33	Cisternas et al. (2013)
			...	...	...	...	...	...	...	Saade et al. (2022)
			NuSTAR	60 371 003 002	2017-12-20	3–24	101.3	30	<2.19	Esparza-Arredondo et al. (2020)
			...	...	...	...	...	...	...	Saade et al. (2022)
NGC 3628	11:20:16.92	+13:35:20.59	*Chandra*	395	1999-11-03	0.5–8	1.8	5	<3.60	...
			...	...	...	...	...	20	131.5 ± 10.3	...
			...	2039	2000-12-02	0.5–8	58.0	5	5.35 ± 0.34	González-Martín et al. (2009)
			...	...	...	...	...	20	71.36 ± 1.25	González-Martín et al. (2009)
			NuSTAR	60 371 004 002	2017-12-23	3–24	100.5	20	4.15 ± 0.25	Esparza-Arredondo et al. (2020)
			...	...	...	...	...	...	...	Osorio-Clavijo et al. (2022)
NGC 4565	12:36:20.78	+25:59:15.58	*Chandra*	404	2000-06-30	0.5–8	2.8	3	50.83 ± 4.26	Wu et al. (2002)
			...	3950	2003-02-08	0.5–8	59.2	3	37.83 ± 0.81	Chiaberge et al. (2006)

Note. (1) Galaxy name; (2)−(3) AGN position that was used to extract the spectra, mostly from *Chandra*, expect for NGC 1792; (4) observatory; (5) observation identification number; (6) observation UT start date; (7) energy band in keV; (8) the net (clean) exposure time in ks; (9) radius of circular region used to extract the spectra; (10) net count rate within the extraction region in the given energy band in units of 10^{-3} cts s^{-1}. The net exposure times and count rates for *NuSTAR* and *XMM-Newton* are the total values from the FPMs, and EPIC cameras, respectively. (11) Previous work that has analysed the same data.

Table 3. X-ray spectral fitting results.

Name	Facility	Model	Energy Band (keV)	Γ	log $N_{\rm H}$ ($\rm cm^{-2}$)	log $L_{2-10,\rm obs}$ ($\rm erg\ s^{-1}$)	log $L_{2-10,\rm int}$ ($\rm erg\ s^{-1}$)	χ^2 or C-stat/d.o.f	Ref.
(1)	(2)	(3)	(4)	(5)	(6)	(7)	(8)	(9)	(10)
				This work					
NGC 0613	*C*	(ZWABS∗ZPOW)+ZGAU	0.5–8	$2.24^{+1.29}_{-1.06}$	$23.58^{+0.14}_{-0.16}$	40.47	41.05	89/88 (χ^2)	...
	C	BORUS	0.5–8	1.8[f]	$23.52^{+0.05}_{-0.04}$	40.49	41.05	80/74 (χ^2)	...
	C	MYTORUS	0.5–8	$2.03^{+0.22}_{-0.28}$	$23.54^{+0.05}_{-0.04}$	40.47	41.12	105/82 (χ^2)	...
NGC 1792[a]	$C+N$	ZWABS(ZCUTOFFPOW)	0.5–24	1.80[f]	≤22.39	≤38.80	≤38.80	99/129 (C-stat)	...
NGC 3621	$XMM+N$	ZWABS(ZCUTOFFPOW)	0.5–24	1.60 ± 0.10	$20.54^{+0.19}_{-0.33}$	39.64	39.83	457/423 (χ^2)	...
	C	ZWABS(ZPOW)	0.5–8	1.80[f]	≤ 21.25	37.53	37.53	20/21 (C-stat)	...
NGC 3627	$C+N$	ZWABS(ZPOW)	0.5–24	1.80[f]	$22.10^{+0.18}_{-0.24}$	38.64	38.66	22/13 (χ^2)	...
	$C+N$	BORUS	0.5–24	1.80[f]	$22.71^{+0.99}_{-0.42}$	38.70	38.72	16/12 (χ^2)	...
	$C+N$	MYTORUS	0.5–24	1.80[f]	$22.67^{+1.02}_{-0.39}$	38.70	38.72	16/12 (χ^2)	...
NGC 3628	$C+N$	ZWABS(ZPOW)	0.5–24	$2.01^{+0.29}_{-0.24}$	$22.10^{+0.16}_{-0.17}$	39.84	39.86	218/181 (χ^2)	...
	C	ZWABS(ZPOW)	0.5–8	$2.00^{+0.44}_{-0.39}$	$21.87^{+0.17}_{-0.19}$	38.72	38.73	12/12 (χ^2)	...
NGC 4565	*C*	ZWABS(ZPOW)	0.5–8	1.88 ± 0.04	$21.34^{+0.08}_{-0.09}$	39.43	39.44	90/86 (χ^2)	...
				Past studies					
Circinus	$C+XMM+N$	MYTORUS	2–79	2.40 ± 0.03	$24.87^{+1.68}_{-0.20}$	40.45	42.57	2785/2637 (χ^2)	Arévalo et al. (2014)
ESO121-G6	$C+N$	BNTORUS	0.5–50	$1.89^{+0.11}_{-0.06}$	23.29 ± 0.02	40.53	41.01	368/317 (χ^2)	Annuar et al. (2020)
NGC 0660[b]	$C+N$	MYTORUS	0.5–30	1.8[f]	$23.78^{+0.18}_{-0.22}$	39.07	39.76	181/186 (C-stat)	Annuar et al. (2020)
NGC 1068	$C+XMM+N+$BAT	MYTORUS	2–195	$2.10^{+0.06}_{-0.07}$	$25.00^{+u}_{-0.01}$	41.21	43.30	1899.2/1666 (χ^2)	Bauer et al. (2015)
NGC 1448	$C+N$	MYTORUS	0.6–40	1.9[f]	$24.65^{+u}_{-0.22}$	38.95	40.88	429/440 (C-stat)	Annuar et al. (2017)
NGC 4051	*N*	MYTORUS	2–70	2.33 ± 0.05	$20.06^{+0.05}_{-0.04}$	41.09	41.09	569/537 (χ^2)	Turner et al. (2017)
NGC 4945	$C+S+N$	MYTORUS	0.5–79	1.96 ± 0.07	$24.54^{+0.02}_{-0.01}$	39.48	42.76	1118/1055 (χ^2)	Puccetti et al. (2014)
NGC 5033	$XMM+N+BAT$	BORUS	0.5–195	1.74 ± 0.02	$20.00^{+0.09}_{-u}$	41.13	41.13	1177/1058 (χ^2)	Diaz et al. (2023)
NGC 5128	$XMM+N$	MYTORUS	3–78	1.82 ± 0.01	$23.04^{+0.06}_{-0.01}$	41.73	42.00	1667/1536 (χ^2)	Fürst et al. (2016)
NGC 5194	$C+N$	MYTORUS	0.6–50	1.8 ± 0.3	$24.85^{+0.15}_{-0.24}$	38.99	40.77	169.3/155 (χ^2)	Xu et al. (2016)
NGC 5195	$C+N$	ZWABS(ZPOW)	0.5–24	$2.12^{+0.61}_{-0.23}$	$22.07^{+0.40}_{-0.81}$	38.80	38.82	226/243 (C-stat)	Annuar et al. (2020)
NGC 5643	$C+XMM+N+BAT$	MYTORUS	0.5–100	$2.10^{+0.04}_{-0.02}$	$24.76^{+u}_{-0.10}$	40.20	41.95	570/471 (χ^2)	Annuar et al. (2015)
NGC 6300[c]	*N*	MYTORUS	3–40	$1.51^{+0.04}_{-0.05}$	$23.08^{+0.01}_{-0.03}$	41.51	41.83	812/819 (χ^2)	Jana et al. (2020)

Notes. Column (1) AGN name; (2) X-ray facilities used in the analysis (BAT: *Swift*-BAT; C: *Chandra*; N: *NuSTAR*; XMM: *XMM-Newton*; XRT: *Swift*-XRT); (3) Best-fitting models to the spectra; (4) Energy band used in the analysis in keV; (5) Best-fitting photon index; (6) Logarithm of the best-fitting line-of-sight column density measured in $\rm cm^{-2}$; (7-8) Logarithm of the observed and absorption-corrected 2–10 keV luminosities, respectively, in $\rm erg\ s^{-1}$; (9) Fit statistic results and approach; (10) Reference for the results.

[f] fixed

[a] The observed and intrinsic luminosity for NGC 1792 should be regarded as upper limits as the AGN was not detected in either of the *Chandra* or *NuSTAR* observations. However we also note that the AGN could be extremely CT, causing it to not be detected in both X-ray observations (see Section 4.2).

[b] The column density and intrinsic luminosity for NGC 660 should be regarded as lower limits due to strong evidence for CT obscuration (see Annuar et al. 2020).

[c] NGC 6300 has been demonstrated to be variable between different X-ray observations (Jana et al. 2020). Here, we quote the results from the most recent *NuSTAR* data. We note, however, that the column density value has been consistent between all observations.

from this extraction region is 45.1 $\times$ 10^{-3} counts s^{-1} ($\sim$2200 counts), allowing us to perform a relatively detailed modelling of the spectrum.

We modelled the spectrum using three models: an absorbed power-law, MYTORUS and BORUS. There is an excess of emission at $\sim$6.4 keV, suggesting the presence of an Fe Kα line, indicating heavy obscuration. We therefore added a GAUSSIAN component to our power-law model in order to simulate this emission-line. In addition, we also found that the spectrum required a soft power-law and two APEC components to simulate the thermal emission at low energy. Based on our analyses, we found that all three models provide comparably good fits to the data, with the BORUS model having the lowest reduced χ^2 value of $\sim$ 1.1. However, we had to fix the photon index for this model to 1.8 (Ricci et al. 2017a) as it was unconstrained. The photon indices measured by the other two models are consistent with the typical intrinsic value found for AGN (e.g. Burlon et al. 2011; Ricci et al. 2017a). All three models provided an $N_{\rm H}$ value of $\approx$3.0 $\times$ 10^{23} cm^{-2}, indicating that the AGN is heavily obscured but not CT (see Table 3). This is in agreement with was what found by Castangia et al. (2013) using *XMM-Newton* data. The plasma temperatures measured by the two APEC components in the power-law model are $kT_1 = 0.51^{+0.14}_{-0.13}$ keV and $kT_2 = 1.14^{+0.12}_{-0.11}$ keV, respectively, consistent with Castangia et al. (2013). We show the modelled spectrum of NGC 613 fitted by all three models in Fig. 3.

4.2 NGC 1792

NGC 1792, located at a distance of 12.5 Mpc, is classified as an HII galaxy in the optical (Veron-Cetty & Veron 1986). The source has been observed at high spatial resolution at 12μm by Gemini/T-ReCS ($t_{\rm exp}$ = 319 s), but was not detected. In X-rays, it has only been previously observed by *XMM-Newton* (2007-03-29; ObsID 0403070301; $t_{\rm exp}$ = 23.3 ks). The *XMM-Newton* observation revealed diffuse soft emission at the nuclear position of the galaxy, with no clear indication of a point source. However, a [Ne V] emission-line is clearly detected at the central part of the galaxy in GA09, indicating that it hosts an AGN.

4.2.1 *X-ray observations and spectral analysis*

We observed NGC 1792 with *Chandra* in 2016 for 19.8 ks (2016-11-23; ObsID 19524), to provide complete *Chandra* coverage for our sample. However, an X-ray source associated with the nuclear position of NGC 1792 was not detected. The nearest source to the 2MASS nuclear position of the galaxy is detected $\sim$ 5 arcsec away. The upper limit fluxes measured at this central position are 7.6 $\times$ 10^{-15} erg s^{-1} cm^{-2} and 8.54 $\times$ 10^{-15} erg s^{-1} cm^{-2} at 0.5–2 keV and 2–8 keV, respectively. We also managed to obtain *NuSTAR* observation of the source in 2018 for 22.9 ks (2018-05-13; ObsID 60371001002). However, no strong emission was detected near the central position of the galaxy using the detection technique adopted in other *NuSTAR* studies of faint sources (significance $\lesssim 2.6\sigma$; e.g. Luo et al. 2013; Lansbury et al. 2014; Stern et al. 2014). We show *Chandra* and *NuSTAR* RGB images of NGC 1792 in Fig. 4.

We extracted X-ray spectra of the source anyway to obtain a measurement of $N_{\rm H}$ that could be used as an estimation for the AGN column density. The spectra was extracted using a circular extraction region with 20 arcsec radius, centred on the 2MASS position of the galaxy. This region size corresponds to $\sim$ 30 per cent of the *NuSTAR* encircled energy fraction, and the size was chosen to minimize contamination of off-nuclear sources. There are no significant differences between the *Chandra* and *NuSTAR* spectra. We therefore fitted the two spectra simultaneously using a simple absorbed cutoff power-law model to simulate the AGN emission, with an additional APEC component to model the thermal emission at low-energy. In addition, there are three off-nuclear sources detected within the extraction region in the full *Chandra* 0.5–8 keV band. We included the power-law components for two of these sources (ON 2 and 3) into our model. The component for ON 1 was not included as its contribution was relatively insignificant, although it is more significant than the AGN emission, which is completely undetected. Under this assumption, the observe AGN luminosity would be much lower than the measured value.

The photon index was fixed to 1.8 as we were not able to constrain it. We obtained a good fit to the data (reduced $\chi^2 \sim 1.3$) that provided an upper limit of $N_{\rm H} \leq 2.5 \times 10^{22}$ cm^{-2}, suggesting that it is just mildly obscured at most. Note that, the AGN could also be extremely CT, causing it to not be detected in our X-ray data. The observed luminosity measured for the AGN using this model is 6.30 $\times$ 10^{38} erg s^{-1}, which should be taken as an upper limit. The intrinsic luminosity of the source however, could be higher than this observed luminosity if it is indeed heavily CT. The plasma temperature measured by the APEC component is $kT = 0.75^{+0.15}_{-0.41}$ keV. The best-fit spectra for the source are shown in Fig. 4.

4.3 NGC 3621

NGC 3621 is a late-type (Sd) bulgeless spiral galaxy located at a distance of 6.6 Mpc. The presence of an AGN in the galaxy was initially discovered by the detection of the [Ne V] emission-line from *Spitzer* spectroscopic observation (Satyapal et al. 2007), which was also later confirmed by GA09. Optical spectroscopy later identified the presence of a Seyfert 2 nucleus (Barth et al. 2009). A *Chandra* observation also detected a weak X-ray point source coincident with the nucleus of the galaxy, adding to the growing evidence that black holes can in fact form and grow in a bulgeless disc galaxy (Gliozzi et al. 2009). *Hubble Space Telescope (HST)* images for this object reveal a bright and compact nuclear star cluster, providing evidence that black holes can be found inside some nuclear star clusters (Barth et al. 2009). The *Chandra* observation also reveals the presence of two potential ULXs located almost symmetrically 20 arcsec away from the centre. However, Gliozzi et al. (2009) did not perform X-ray spectral fitting on the AGN due to low count rates. Despite this, they concluded that the collective evidence from optical and infrared spectroscopic results provides strong support that NGC 3621 harbours a buried AGN. The AGN is not detected in the *Swift*-BAT survey (Oh et al. 2018), and has not been observed at high angular resolution at mid-IR wavelengths.

4.3.1 *X-ray observations and spectral fitting*

Prior to our work, NGC 3621 had only been observed in X-rays by *Chandra* (see above). We obtained simultaneous *NuSTAR* (2017-12-15; ObsID 60371002002) and *XMM-Newton* (2017-12-16; ObsID 0795660101) observations for the galaxy as we expect the AGN and the off-nuclear sources to be spatially resolved by *XMM-Newton*, and the observation could provide higher quality low-energy data to complement the *NuSTAR* data. Osorio-Clavijo et al. (2022) have analysed the *NuSTAR* data alone using the simple reflection models PEXRAV (Magdziarz & Zdziarski 1995) and PEXMON (Nandra et al. 2007). They did not detect any reflection signatures in the spectrum, and measure a column density of $N_{\rm H} = (5.4 \pm 3.6) \times 10^{21}$ cm^{-2},

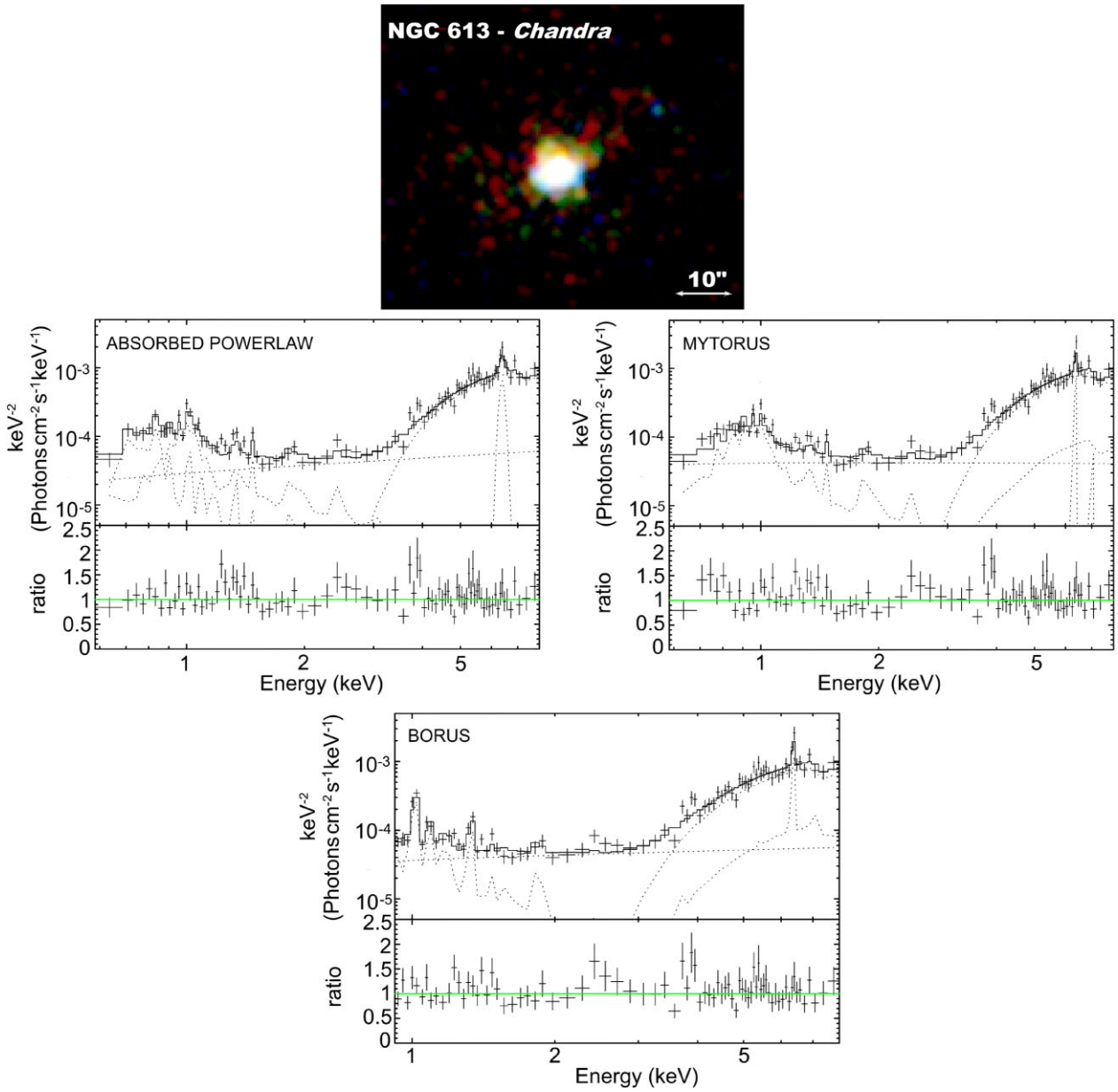

Figure 3. *Top*: *Chandra* RGB images of NGC 613 (Red: 0.5–1 keV, Green: 1–2 keV, Blue: 2–8 keV). The image is smoothed with a Gaussian function of radius 3 pixels, corresponding to 1.5 arcsec. *Bottom*: Best-fitting absorbed power-law model (top left), MYTORUS (top right), and BORUS (bottom) models to the spectra. The top panels show the data and unfolded model in E^2F_E units, whilst the bottom panels show the ratio between the data and the folded model. The model components fitted to the data are shown as dotted curves, and the combined model fits are shown as solid curves.

indicating that the AGN is just mildly obscured. In this paper, we present the *XMM-Newton* observation of the source, and re-analyse the *Chandra* and *NuSTAR* data, taking into consideration contamination from the relatively bright off-nuclear sources in the *NuSTAR* data that could significantly affect the results presented by Osorio-Clavijo et al. (2022) due to the relatively large extraction region used in that study (2 arcmin radius).

The *XMM-Newton* data reveal three sources within 30 arcsec of the centroid position of the galaxy (Fig. 5). However, none is consistent with the *Chandra* position of the AGN (i.e. RA = 11:18:16.51 and Dec. = −32:48:50.78 in the 0.5–8 keV band). Comparing the *Chandra* and *XMM-Newton* images of the galaxy, we found that one of the two off-nuclear sources detected in the older *Chandra* data (ON 2) was not detected in the more recent *XMM-Newton* observation. However, two new off-nuclear sources (ON 3 and 4) emerge in the *XMM-Newton* observation that were not detected in the *Chandra* data. Source ON 1 is clearly visible in the *NuSTAR* data, whilst weak and diffuse emission can be seen at the ON 3 and 4 positions.

Similar to NGC 1792, we performed X-ray spectral analysis on the NGC 3621 data even though it is not significantly detected in both of our *XMM-Newton* and *NuSTAR* data. For this source however, we chose a larger extraction region of 30 arcsec to fully include the off-nuclear source ON 1 emission. Based on our modelling of the off-nuclear sources, we found that a simple absorbed power-law can best describe ON 1 and ON 4, whilst an absorbed cut-off power-law is the best-fitted model for ON 3. However, when we tried to incorporate these components into our modelling to decompose the AGN emission using a simple absorbed power-law model, we could

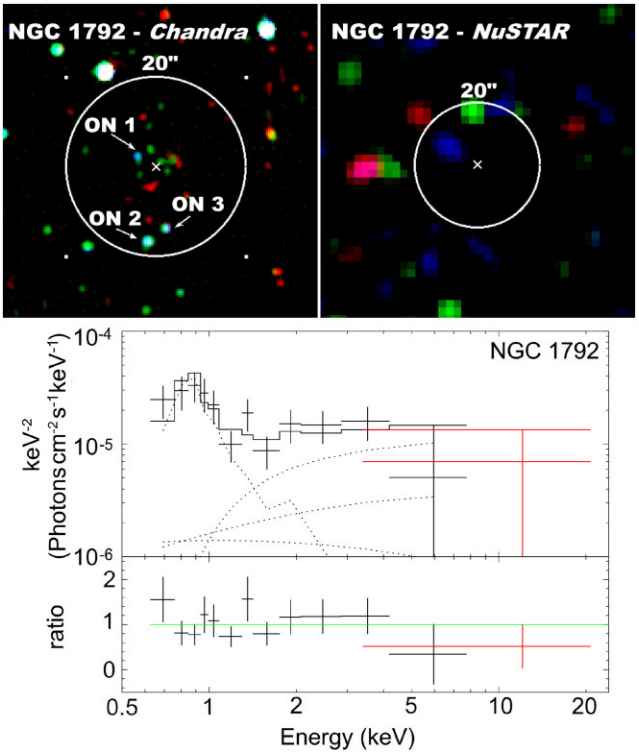

Figure 4. *Top*: *Chandra* and *NuSTAR* RGB images of NGC 1792 (*Chandra* – Red: 0.5–1 keV, Green: 1–2 keV, Blue: 2–8 keV; *NuSTAR* – Red: 3–8 keV, Green: 8–24 keV, Blue: 24–79 keV). The off-nuclear sources detected within the 20 arcsec-radius extraction region in *Chandra* are labelled ON 1, ON 2, and ON 3. The images are smoothed with a Gaussian function of radius 3 pixels, corresponding to 1.5 and 7.4 arcsec for *Chandra* and *NuSTAR*, respectively. *Bottom*: Best-fitting model to the combined *Chandra* (black) and *NuSTAR* (red) data. The data have been rebinned to a minimum of 3σ significance with a maximum of 500 bins for visual clarity. The top panel shows the data and unfolded model in E^2F_E units, whilst the bottom panel shows the ratio between the data and the folded model. The spectra were fitted using an absorbed power-law model to simulate the AGN emission, and two cut-off power law components to model the off-nuclear sources, ON 2 and ON 3. ON 1 was not included in the spectral fitting as its contribution was found to be insignificant. The model components fitted to the data are shown as dotted curves, and the combined model fit is shown as a solid curve.

not constrain the parameters. We therefore just modelled the total spectra using an absorbed cutoff power-law model as it clearly turns down at high energy. Indeed, our model measured a cut-off energy of $E \sim 12$ keV. The photon index and column density measured towards the AGN are $\Gamma = 1.60 \pm 0.10$ and $N_{\rm H} = (3.5 \pm 1.9) \times 10^{20}$ cm^{-2}, respectively, suggesting that the AGN is unobscured, with a 2–10 keV intrinsic luminosity of 4.37×10^{39} erg s^{-1}.

The measured $N_{\rm H}$ value is consistent with that constrained by the *Chandra* observation using a much smaller aperture region of 3 arcsec, clearly isolating the AGN emission from any off-nuclear sources. Based on our analysis of the *Chandra* data using a simple power-law model with a photon index 1.8, we measured a column density upper limit towards the AGN of $N_{\rm H} \leq 1.8 \times 10^{21}$ cm^{-2} with 2–10 keV intrinsic luminosity of 3.39×10^{37} erg s^{-1}. As we believe that the results from the *Chandra* data are more reliable (due to actual detection of the AGN and lack of contamination), we therefore used the results from these data throughout this paper (see Table 3).

In Fig. 5, we show the best-fit spectra using the *Chandra*, *XMM-Newton* and *NuSTAR* data.

4.4 NGC 3627

NGC 3627 is a a spiral galaxy (Sb) located at a distance of 10 Mpc. It is a member of the Leo triplet galaxies and is in tidal interaction with NGC 3623 and NGC 3628. In the optical, the AGN has been variously identified as a LINER (e.g. Véron-Cetty & Véron 2006; GA09), transition object (e.g. Dudik et al. 2005) and Seyfert 2 (e.g. Brightman & Nandra 2011), depending on the diagnostics used. In X-rays, the presence of an AGN has also been in debate, mainly due to the lack of a clearly resolved nuclear point source and faint flux emission in *Chandra* data (e.g. Panessa et al. 2006; Cisternas et al. 2013). It is also not detected in the *Swift*-BAT survey (Oh et al. 2018). However, the high ionization [Ne V] line was detected by GA09, providing strong evidence for the presence of an AGN in the galaxy. Using high angular resolution mid-IR observations by VLT-VISIR, complex extended emission was detected in the nuclear region, in which a compact source cannot be clearly identified (Asmus et al. 2014).

González-Martín et al. (2009) suggested that NGC 3627 is a CT AGN candidate on the basis of its $L_{2-10}/L_{[\rm OIII]}$ ratio using the X-ray luminosity estimated from *XMM-Newton* observation (see also Fig. 12). In contrast, using the same data, Brightman & Nandra (2008) measured an ionized absorption column density of $\approx 5.0 \times 10^{21}$ cm^{-2} toward the source, suggesting that it might actually be an unobscured AGN.

4.4.1 X-ray observations and spectral fitting

NGC 3627 has been observed multiple times in X-rays using, e.g. *Chandra* and *XMM-Newton*. We acquired a *NuSTAR* observation of the galaxy in 2017 (2017-12-20; ObsID 60371003002) due to evidence from multiwavelength diagnostics that it could be CT (e.g. González-Martín et al. 2009; see also Section 5.1, and Figs 12 and 13). Our *NuSTAR* data were fitted by Esparza-Arredondo et al. (2020) using a simple model partial covering absorber component. Based on their analysis, they measured a CT column density of $N_{\rm H} = (1.8 \pm 6.7) \times 10^{24}$ cm^{-2}. After correcting for this absorption, they estimated an intrinsic 2–10 keV luminosity of $L_{2-10,\rm int} < 1.58 \times 10^{42}$ erg s^{-1}. When compared to its [O III] and 12μm luminosities, they found the source to be underluminous in X-ray, suggesting that the AGN is in the early fading stage of the AGN duty cycle. This is supported by Saade et al. (2022) who also analysed the *NuSTAR* data of the AGN together with *Chandra* data to account for multiple brighter off-nuclear sources within the *NuSTAR* beam (that could also heavily contaminate the *XMM-Newton* data analysed by previous studies). In contrast however, they did not find evidence for obscuration due to the absence of a reflection component, and therefore did not provide a column density measurement. Given the significantly low intrinsic luminosity of the AGN in X-ray as compared to the mid-IR, they also suggest that the AGN is fading and recently deactivated at least ∼90 yr ago.

Here, we re-analyse the *NuSTAR* data, together with archival *Chandra* data to provide a measurement of its column density using physically motivated torus models. Due to the complexity of the central region of the galaxy as shown in the Chandra data in Figure 6, with multiple off-nuclear sources near the AGN, we took a different approach in analysing the AGN spectra for this source. We extracted the *NuSTAR* spectra using a circular region with 30 arcsec radius,

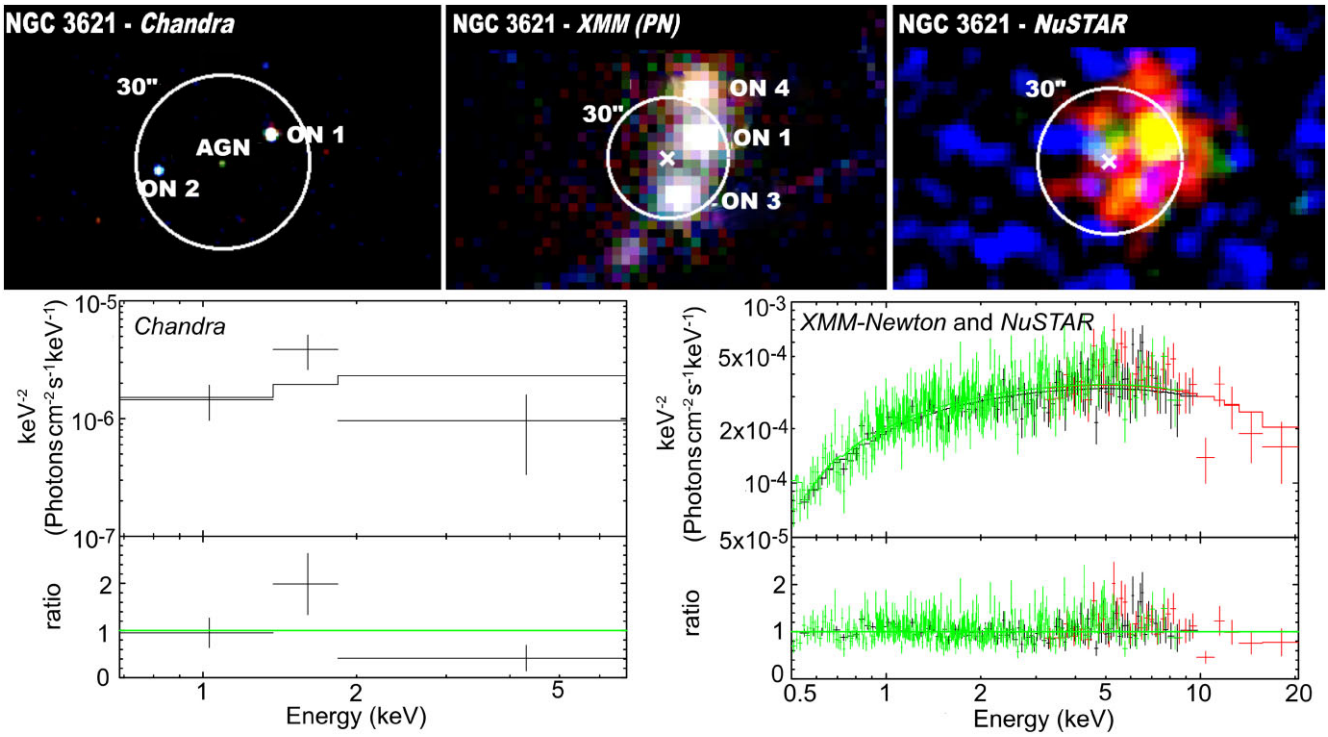

Figure 5. *Top*: *Chandra*, *XMM-Newton* and *NuSTAR* RGB images of NGC 3621 (*Chandra* – Red: 0.5–1 keV, Green: 1–2 keV, Blue: 2–8 keV; *XMM-Newton* – Red: 0.5–1 keV, Green: 1–2 keV, Blue: 2–10 keV; *NuSTAR* – Red: 3–8 keV, Green: 8–24 keV, Blue: 24–79 keV). The off-nuclear sources which are detected within the 30 arcsec-radius extraction region in *Chandra* and *XMM-Newton* are labelled ON 1, ON 2, ON 3, and ON 4. *Bottom*: Best-fitting absorbed power-law model to the *Chandra* spectrum extracted from a small 3 arcsec region corresponding to the AGN (left), and to the combined *NuSTAR* (red) and *XMM-Newton* data (black – PN; MOS – green). Figure description is the same as Fig. 4.

whilst for the *Chandra* data, we isolated the AGN emission using a smaller circular region of 2 arcsec radius. This is because the AGN emission starts to dominate over most of the off-nuclear sources in the energy in the high energy band of the *Chandra* data. The *NuSTAR* data also seem to be consistent with the *Chandra* data if we were to extrapolate it into the *NuSTAR* band (see Annuar et al. 2020 for a similar case in NGC 660). Based on a simple modeling approach using an absorbed power-law model, we measured a column density of $N_{\rm H} = (1.3 \pm 0.7) \times 10^{22}$ cm^{-2}. We therefore proceed with the MYTORUS and BORUS models which indeed confirm a column density of this magnitude, indicating a mildly obscured AGN (see Figure 6). These results broadly agree with the conclusion of Saade et al. (2022) and argue against NGC 3627 harbouring a CTAGN. The 2–10 keV intrinsic luminosity of the AGN is $\sim 5 \times 10^{38}$ erg s^{-1} (see Table 3).

4.5 NGC 3628

NGC 3628 is an edge-on Sb spiral located at $D = 10$ Mpc with distorted dust lanes due to its interaction with the other two galaxies in the Leo Triplet; i.e, NGC 3623 and NGC 3627. The nucleus is classified as LINER in the optical (e.g. GA09), and has been detected in radio (e.g. Filho, Barthel & Ho 2000; Nagar, Falcke & Wilson 2005) and *Chandra* (González-Martín et al. 2009). However, the *Chandra* image shows a diffuse central source rather than a point source, which led González-Martín et al. (2009) to infer that the galaxy does not host an AGN. It is also not detected at 12μm using high angular resolution observations by VLT-VISIR, and Asmus et al. (2014) therefore concluded that any AGN contribution to the mid-IR emission of the central ∼0.2 kpc is minor. However, GA09 detected the [Ne V] line emission at a 3σ significance level from the galaxy, indicating the presence of an AGN. The AGN has not been detected in the *Swift*-BAT survey (Oh et al. 2018).

4.5.1 *X-ray observations and spectral fitting*

NGC 3628 has been observed multiple times in X-rays by *Chandra* and *XMM-Newton*. These data show several nearby, off-nuclear sources which dominate at low energies. There is a lack of a strong indication that it is highly obscured. However, motivated by the lack of reliable high-energy archival data, we obtained a *NuSTAR* observation of NGC 3628 in 2017 (2017-12-23; ObsID 60371004002). The *NuSTAR* data were analysed by Esparza-Arredondo et al. (2020) using a simple model which includes a partial covering absorber component. They found a column density of $\sim 2 \times 10^{23}$ cm^{-2}, indicating a heavily obscured AGN. Osorio-Clavijo et al. (2022) also analysed the *NuSTAR* data using reflection models (i.e. PEXRAV and PEXMON). However, they did not find any signs of reflection in the spectrum, and measured a column density limit of $N_{\rm H} < 1.2 \times 10^{22}$ cm^{-2}, indicating that the AGN is most likely unobscured.

We analyse the *NuSTAR* data again, together with its archival *Chandra* data to help account for off-nuclear source contributions in the *NuSTAR* spectrum that could significantly affect the results presented by both Esparza-Arredondo et al. (2020) and Osorio-Clavijo et al. (2022) due to the relatively large extraction region used in these studies (1 and 2 arcmin, respectively). The *Chandra* data reveal that the AGN is embedded in diffuse emission with several off-

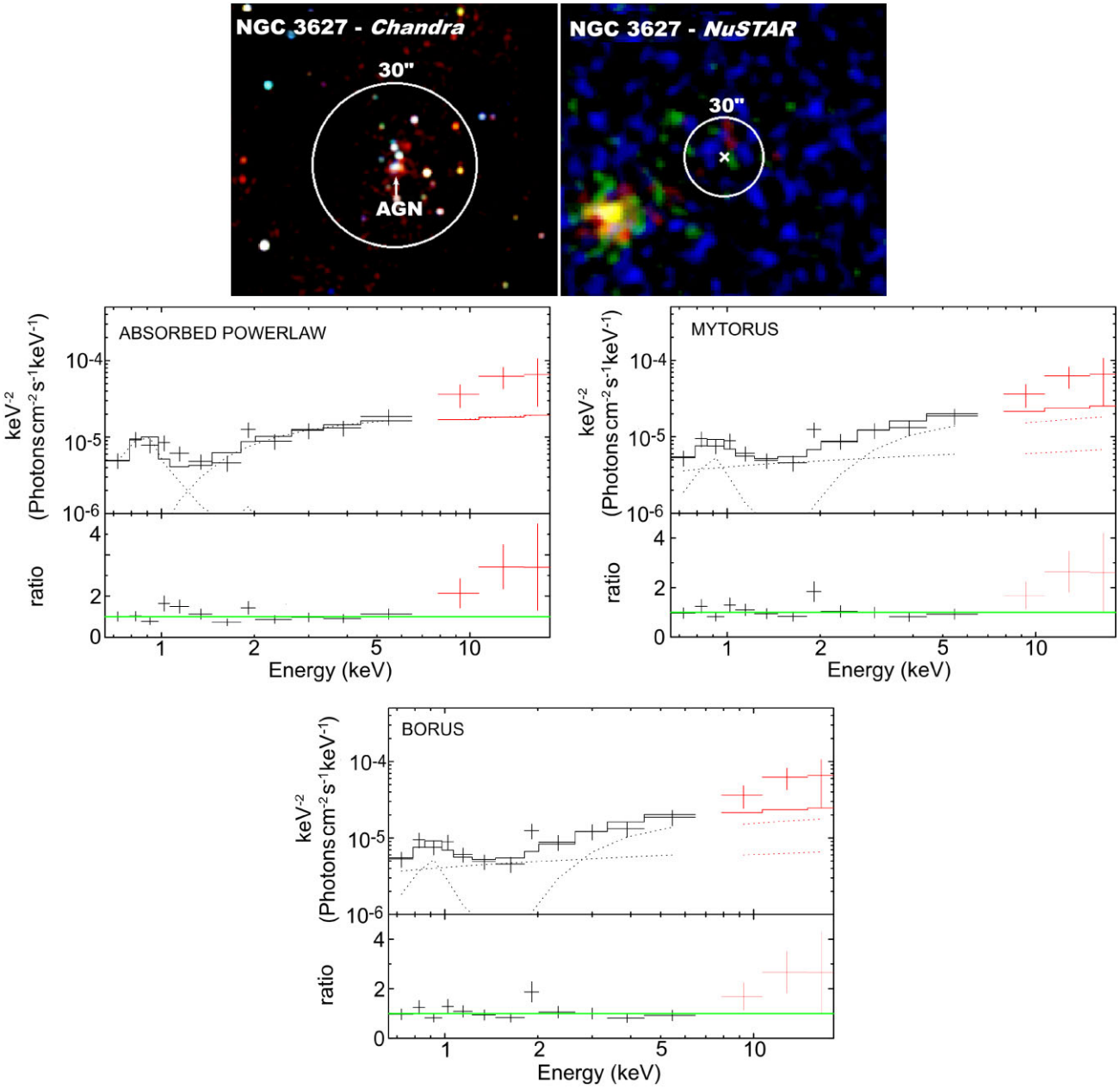

Figure 6. *Top*: *Chandra* and *NuSTAR* RGB images of NGC 3627. *Bottom*: Best-fitting absorbed power-law (top left), MYTORUS (top right) and BORUS (bottom) models to the combined *NuSTAR* (red) and *Chandra* (black) data. Figure description is the same as Fig. 4.

nuclear point sources detected at 0.5–8 keV band within a 20 arcsec-radius of the AGN, of which two are detected in the 2–8 keV band (see Fig. 7). Whilst one of these high-energy emitting off-nuclear sources is visible in the *NuSTAR* data (ON 1), the AGN seems to be undetected. We firstly analysed the source spectra extracted from a 20 arcsec-radius circular region using a simple absorbed power-law model. Based on this, we measured a column density of $N_{\rm H} = (1.3 \pm 0.6) \times 10^{22}$ cm^{-2}, with $L_{2-10,\rm int} = 6.92 \times 10^{39}$ erg s^{-1}. This is in agreement with that measured using just the *Chandra* data with a smaller aperture region of 5 arcsec radius, minimizing contamination from much of the off-nuclear sources; i.e. $N_{\rm H} = (7.4 \pm 3.6) \times 10^{21}$ cm^{-2}, with $L_{2-10,\rm int} = 5.24 \times 10^{38}$ erg s^{-1}. As with NGC 3621, we adopt the results from the *Chandra* data for this source throughout this paper as well as they are more reliable (see Table 3).

4.6 NGC 4565

NGC 4565 is an edge-on spiral galaxy (Sb) located at a distance of $D = 10$ Mpc, with a nucleus classified as Seyfert 2 (Ho et al. 1997). Despite the optical classification, the nuclear source was found to be unabsorbed by Chiaberge et al. (2006) with a column density of $N_{\rm H} = (2.5 \pm 0.6) \times 10^{21}$ cm^{-2} and intrinsic luminosity of $L_{2-10,\rm int} \approx 2.5 \times 10^{39}$ erg s^{-1}, measured using *Chandra* data. The luminosity measured is comparable with that obtained by other studies using *XMM-Newton* data (Wu et al. 2002; Cappi et al. 2006). In addition, Chiaberge et al. (2006) found that the spectral energy distribution (SED) of the AGN shows no sign of a UV bump or thermal IR emission. The Eddington ratio determined for the AGN is also very low; i.e. $\sim 10^{-6}$, and its position on the diagnostic planes for low-luminosity AGN suggests that the optical nucleus is disc-dominated, instead

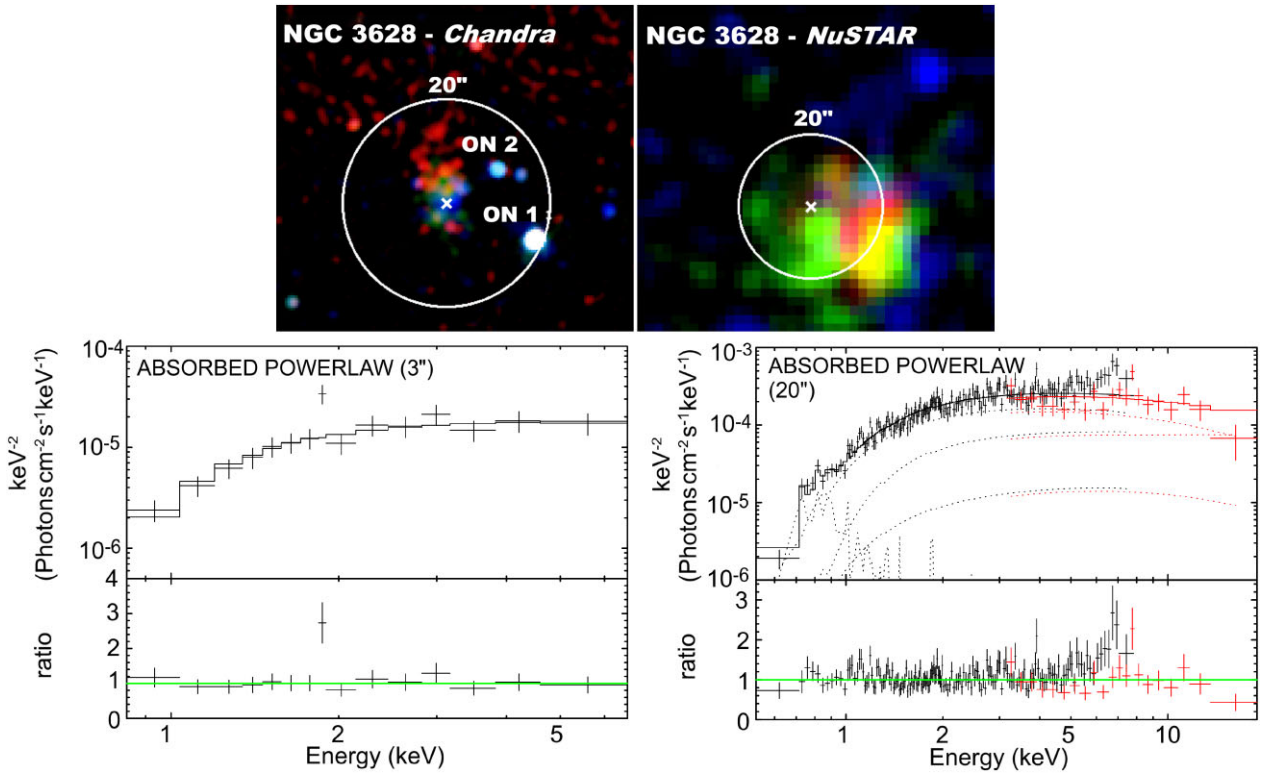

Figure 7. *Top*: *Chandra* and *NuSTAR* RGB images of NGC 3628. The off-nuclear sources which were detected significantly detected within the 20 arcsec-radius extraction region in *Chandra* are labelled as ON 1 and ON 2. *Bottom*: Best-fitting absorbed power-law model to the *Chandra* spectrum extracted from a small 3 arcsec radius region (left), and to the combined *NuSTAR* (red) and *Chandra* data (black) extracted with a larger 20 arcsec radius region. The spectra were fitted using an absorbed power-law model to simulate the AGN emission, and two cut-off power-law components to model the off-nuclear sources, ON 1 and ON 2. Figure description is the same as Fig. 4.

of jet-dominated. These pieces of collective evidences indicate that the AGN is undergoing low radiative efficiency accretion (Chiaberge et al. 2006). The AGN has remained undetected in the *Swift*-BAT survey (Oh et al. 2018), and has not been observed at mid-IR using high angular resolution observations.

4.6.1 X-ray observations and spectral fitting

The exact models used to fit the *Chandra* data of NGC 4565 were not specified by Chiaberge et al. (2006). We therefore re-analysed the data for consistency with our modelling technique. The AGN has been observed by *Chandra* twice, and in both data sets, the AGN was clearly detected, free from any contaminants, making its analysis straightforward. This source is one of the two AGN in our sample where we did not pursue a *NuSTAR* observation (see Section 3). We combined the *Chandra* data, and extracted the AGN spectrum from a 3 arcsec-radius circular aperture region. We then modelled it using a simple absorbed power-law model. The best-fit spectrum implies a column density of $N_{\rm H} \sim 2.2 \times 10^{21}$ cm^{-2}, in agreement with that obtained by Chiaberge et al. (2006), confirming that it is an unobscured AGN. The intrinsic luminosity measured is $L_{2-10,\rm int} = 2.75 \times 10^{39}$ erg s^{-1} (see Table 3). Fig. 8 shows the *Chandra* RGB images of the source and the best-fit spectrum.

4.7 Summary

In this section, we have presented the X-ray spectral analysis for the remaining six sources in the $D \leq 15$ Mpc AGN sample, completing our X-ray analysis for the entire sample. Based on our analysis, we found that none of the six AGN is CT. Fig. 9 shows the intrinsic 2–10 keV luminosity as a function of $N_{\rm H}$ for our sample and the *Swift*-BAT AGN sample. Based on the figure, we can deduce that all of our sources with $L_{2-10,\rm int} < 10^{40}$ erg s^{-1} are unobscured or just mildly obscured; i.e. $N_{\rm H} \lesssim 10^{22}$ cm^{-2}, with the exception of the CT AGN candidate, NGC 660, which has $L_{2-10,\rm int} \gtrsim 5.8 \times 10^{39}$ erg s^{-1} and $N_{\rm H} \gtrsim 6.0 \times 10^{23}$ cm^{-2} (see Table 3 and Annuar et al. 2020). This may indicate that at the low-luminosity of $L_{2-10,\rm int} < 10^{40}$ erg s^{-1}, the AGN torus is not well developed, supporting findings by multiple past studies (e.g. Maoz et al. 2005; Elitzur & Shlosman 2006; Hönig & Beckert 2007; Elitzur & Ho 2009; González-Martín et al. 2017).

5 COMPARISONS WITH MULTIWAVELENGTH DATA

In this section, we discuss the multiwavelength properties of the AGN in our sample. We compare the observed and intrinsic 2–10 keV emission measured for the AGN from our X-ray analyses with their optical [O III]λ5007Å emission (Section 4.1), infrared 12μm and [Ne V]λ14.32μm luminosities (Sections 4.2 and 4.3, respectively) in order to complement our X-ray analysis results.

5.1 Optical [O III]λ5007 Å emission

The [O III] emission-line in powerful AGN is mostly produced in the NLR due to photoionization from the central source, and is therefore considered to be a good indicator for the intrinsic flux

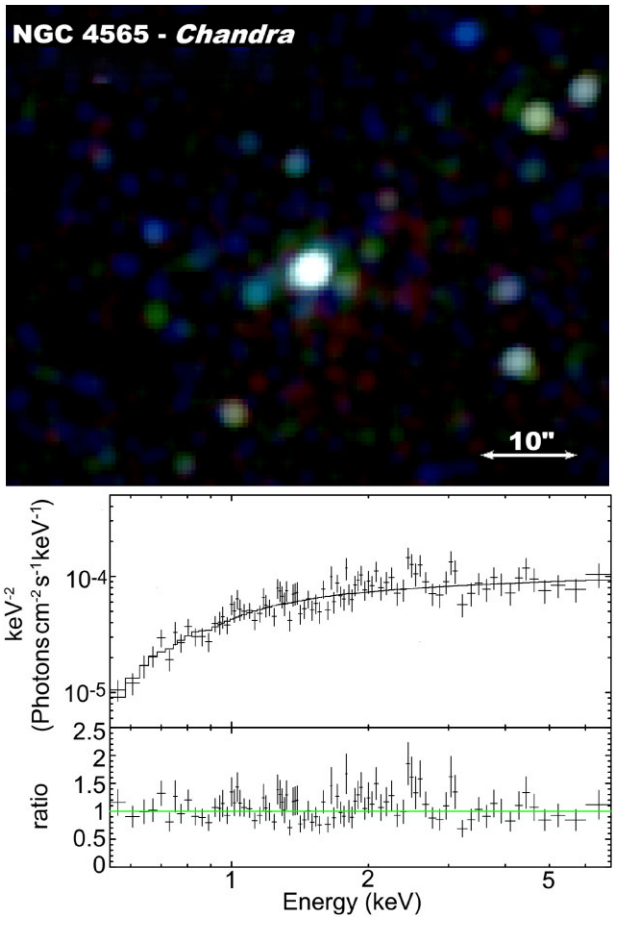

Figure 8. *Top*: *Chandra* RGB image of NGC 4565. *Bottom*: Best-fitting absorbed power-law model to the data. Figure description is the same as Fig. 4.

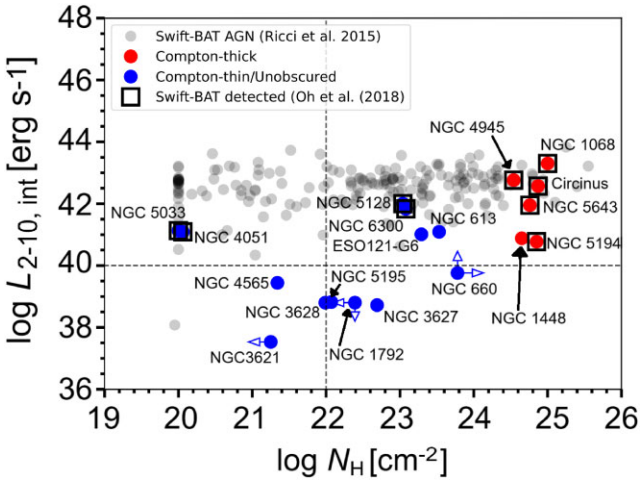

Figure 9. Intrinsic 2–10 keV luminosity versus $N_{\rm H}$ for our sample and the *Swift*-BAT AGN at $D \leq 100$ Mpc.[6] The dashed lines divide the low/high luminosity and obscured/unobscured AGN.

of the AGN. Since the physical scale of this region extends beyond the torus, it does not suffer from nuclear obscuration like the X-ray emission. Optical emission from the NLR however, can be affected by extinction from the host-galaxy. Although in general this can be corrected for using the Balmer decrement (i.e. Hα/Hβ

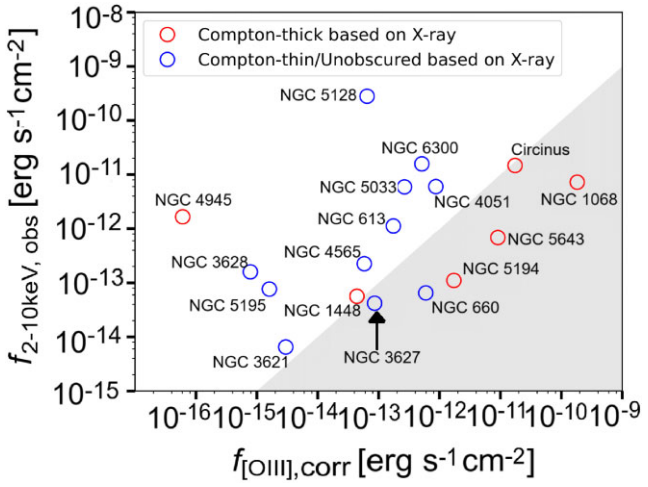

Figure 10. Observed 2–10 keV flux versus [O III]λ5007 Å flux corrected for the Balmer decrement plot for our sample. Red and blue circles marks Compton-thick and Compton-thin AGN on the basis of $N_{\rm H}$ measurements from X-ray spectroscopy, respectively. The grey area indicates a region where $f_{2-10,\rm obs}/f_{\rm [OIII],corr} \leq 1$, which can be used as a CT AGN indicator (Bassani et al. 1999). ESO 121-G6 and NGC 1792 are not plotted in the diagram as they lack good quality optical data.

flux ratio), in extreme cases, the host-galaxy obscuration can be so high that the optical Balmer decrement only provides a lower limit on the extinction (GA09). Fig. 10 shows the comparison between the observed 2–10 keV ($f_{2-10,\rm obs}$) and corrected [O III] flux ($f_{\rm [OIII],corr}$; Table 1) for our AGN sample. Using a sample of Seyfert 2 galaxies with good quality X-ray spectra and therefore reliable $N_{\rm H}$ measurements, Bassani et al. (1999) found that all the CT AGN in their sample have an observed 2–10 keV and intrinsic [O III] flux ratio of $f_{2-10,\rm obs}/f_{\rm [OIII],corr} \lesssim 1$.

Based on this diagnostic technique, we found that most of our X-ray identified CT AGN are selected as CT (4/6, 67^{+33}_{-43} per cent), with the exception of NGC 1448 and NGC 4945. This is due to the fact that the optical emission from these two AGN suffers from significant absorption by their highly inclined host galaxies causing the Balmer decrement to underestimate the NLR extinction (see Annuar et al. 2017 and GA09, respectively). This consequently causes their [O III] luminosities to also be underestimated. Most of the X-ray identified Compton-thin or unobscured AGN (9/11, 82^{+18}_{-39} per cent) lie outside the shaded region in Fig. 10, suggesting that they are not CT, consistent with the results of their X-ray spectral analyses. The remaining sources; i.e. NGC 660 and NGC 3627, are selected as CT using this diagnostic. NGC 660 is found to be at least heavily obscured, and may be CT based upon our X-ray spectral analysis (Annuar et al. 2020). This therefore provides additional evidence in favor of this scenario. On the other hand, NGC 3627 has a Compton-thin column density and has been suggested to be a turned-off AGN (Esparza-Arredondo et al. 2020; Saade et al. 2022).

5.2 Infrared 12μm emission

We also compare the observed X-ray and 12 μm luminosities measured for our sources with the intrinsic X-ray:12μm correlation found by Asmus et al. (2015). The mid-IR continuum emission from AGN is produced by the obscuring torus (Shi et al. 2014) and/or polar dust structures, distributed along the ionization cones (Asmus, Hönig & Gandhi 2016; Hönig 2019). Therefore, it should provide a reliable estimate for the intrinsic luminosity of the AGN. The mid-IR

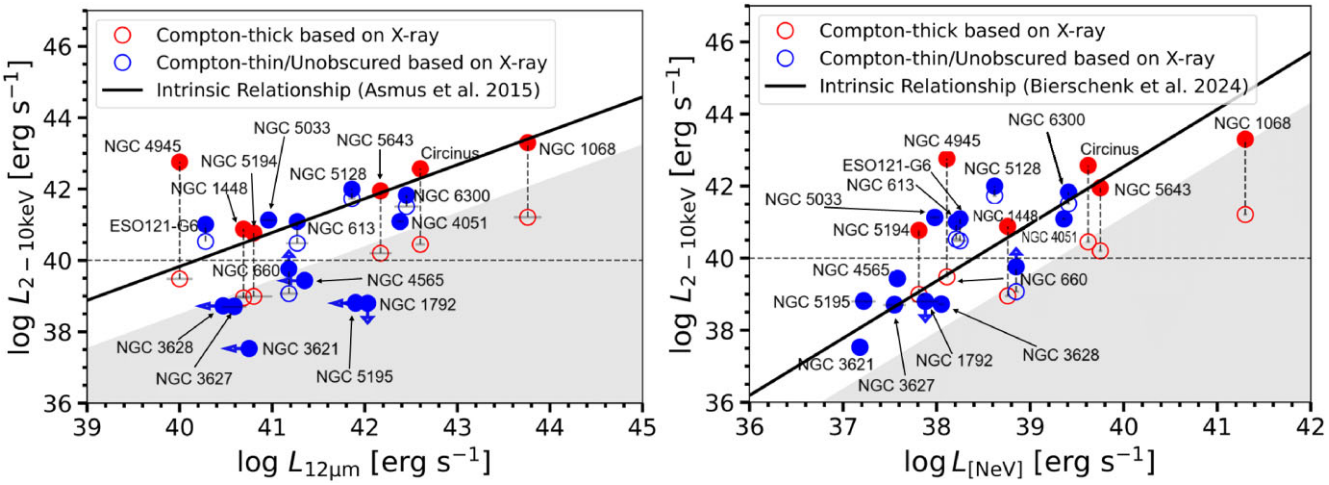

Figure 11. Observed 2–10 keV luminosities versus 12 μm (left) and [Ne V] luminosities (right) for our sample. The solid lines for each plot correspond to the intrinsic relationships derived by Asmus et al. (2015) (scatter, $\sigma \approx 0.3$ dex) and Weaver et al. (2010) (scatter, $\sigma \approx 0.5$ dex), respectively. The symbols are the same as in Fig. 10, with filled circles indicating the intrinsic 2–10 keV luminosities of the AGN. We identified sources which lie $> 25\times$ below the relation (grey region) as CT AGN candidates, following detailed X-ray studies on CT AGN (e.g. Iwasawa, Fabian & Matt 1997; Matt et al. 2000; Baloković et al. 2014; Annuar et al. 2017). The dashed lines divide the low/high luminosity AGN.

emission can also be produced by dust around massive O-B stars; however, the emission from the AGN will typically dominate in this waveband and can be resolved, particularly when high-resolution imaging is used.

The Asmus et al. (2015) X-ray:12μm intrinsic luminosities relationship has been shown to predict the intrinsic X-ray luminosity of AGN very well (see also Horst et al. 2008; Gandhi et al. 2009; Mason et al. 2012). The relationship was derived using mid-IR data from high angular resolution mid-IR observations ($\sim 0\farcs4$) of local Seyfert galaxies. As described earlier, for CT AGN, the X-ray emission that we observe is generally attributed to X-ray photons that are scattered or reflected from the back side of the torus or other circumnuclear material, which consists of just a few percent of the intrinsic power of the AGN in the 2–10 keV band (e.g. Iwasawa et al. 1997; Matt et al. 2000; Baloković et al. 2014; Annuar et al. 2017). Therefore, we can use the Asmus et al. (2015) X-ray:12μm relationship to identify AGN with observed 2–10 keV luminosities that deviate significantly from this intrinsic relationship, suggesting that they are likely to be CT. We show the X-ray:12μm relationship by Asmus et al. 2015 in Fig. 11 (left), with a grey region that we have adopted to select CT AGN candidates, representing a factor of 25× suppression of the X-ray flux (e.g. Rovilos et al. 2014).

We obtain the majority of the 12 μm fluxes (15/19, 79^{+21}_{-30} per cent) from high spatial resolution mid-IR observations (Asmus et al. 2014; Annuar et al. 2017, 2020). The fluxes for the remaining four sources (NGC 1792, NGC 3621, NGC 4565, and NGC 5195) were obtained from *WISE* (Wright et al. 2010), and are used as upper limits due to the lower angular resolution of *WISE*, which means the measurements can suffer significant contamination by the host-galaxy. Based on Fig. 11, we find that most of our bona-fide CT AGN would be selected as CT on the basis of this diagnostic (5/6, 83^{+17}_{-50} per cent), except for NGC 4945. This source is known to be an outlier, having fainter infrared emission than expected, which could be due to low torus covering factor (Madejski et al. 2000; Done et al. 2003; Marinucci et al. 2012; Yaqoob 2012; Puccetti et al. 2014; Marchesi et al. 2019; Boorman et al. 2024b)

Six out of thirteen of our X-ray identified Compton-thin/unobscured AGN would also be selected as CT candidates based on this technique, although the majority are with upper limits for 12 μm measurements, making their classification uncertain on the basis of this method. We note that all of these sources are intrinsically low-luminosity AGN with $L_{2-10,\rm int} < 10^{40}$ erg s^{-1}. NGC 660, which may be CT based upon our X-ray spectral analysis (Annuar et al. 2020) is located very near to the CT region. If we were to adopt the CT solution for this AGN with $L_{2-10,\rm int} > 10^{41}$ erg s^{-1}, it would be in good agreement with the intrinsic correlation (Annuar et al. 2020). These data provide further evidence that the AGN is most likely CT. On the other hand, NGC 3627, which is Compton-thin based on our X-ray analysis, is located at the edge of the CT region. However, this source has been suggested to be deactivated recently, contributing to the lower intrinsic X-ray luminosity measured from the corona, whilst the 12 μm emission from the much larger scale torus could continue to emit (Esparza-Arredondo et al. 2020; Saade et al. 2022).

The fact that the sources that are misidentified as CT AGN have $L_{2-10,\rm int} < 10^{40}$ erg s^{-1} (see Fig. 11 – left) might suggest a few scenarios: (1) the intrinsic correlations derived do not hold at lower AGN luminosities; or (2) flux contamination by non-AGN sources in the mid-infrared wavelength such as stellar activities; or (3) recent deactivation of AGN, contributing to the lower intrinsic X-ray luminosity measured from the corona, whilst the 12 μm emission from the much larger scale torus could continue to emit, such as the case for NGC 3627 (Esparza-Arredondo et al. 2020; Saade et al. 2022); or (4) the AGN are extremely heavily obscured (e.g. $N_{\rm H} \geq 10^{25}$ cm^{-2}) that their X-ray emission are significantly suppressed at all X-ray wavelengths, even the high energy, which could be the case for NGC 1792.

5.3 Infrared [Ne V]λ14.32 μm emission

Our parent sample from GA09 was derived using the detections of the high-ionisation [Ne V] line as an unambiguous indicator of AGN activity in the galaxies. Thus, it should also be a reliable proxy for the intrinsic AGN power. As described earlier, the [Ne V] line is also produced in the NLR, as with the [O III] emission-line. However, since it is produced in the mid-IR ($\lambda = 14.32$ μm), it is less likely to be affected by extinction through the host-galaxy, unlike the optical [O

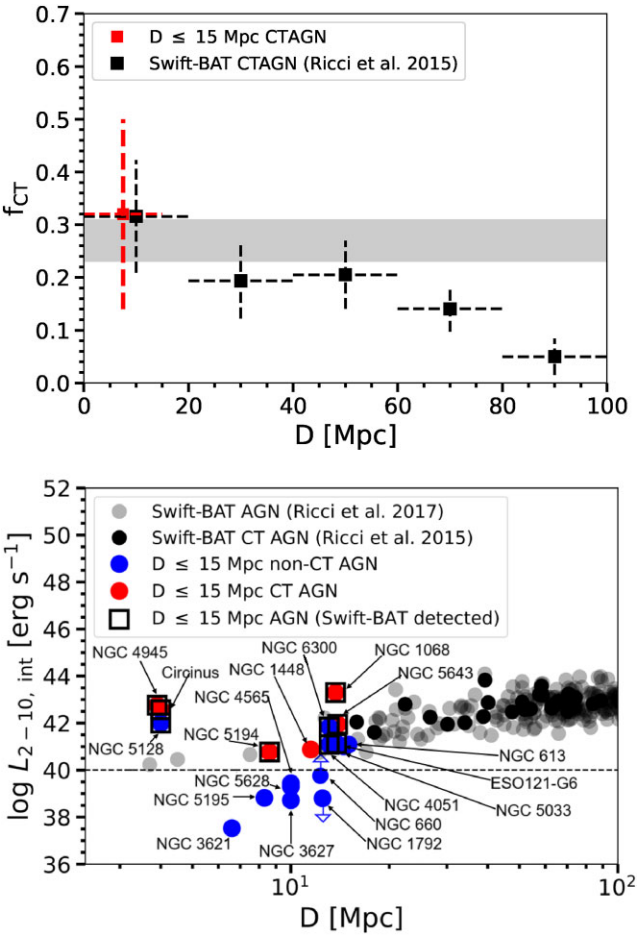

Figure 12. *Top*: CT AGN fraction as a function of distance for our sample (red) and the *Swift*-BAT AGN located within 100 Mpc (black). The grey region shows the range of the intrinsic CT AGN fraction inferred using the whole *Swift*-BAT AGN sample (i.e. over the entire range of X-ray luminosity; log $L_{14-195} = 40$–46 erg s^{-1}; Ricci et al. 2015). *Bottom*: Intrinsic 2–10 keV luminosities for the CT AGN in our sample[6] (red) and the entire *Swift*-BAT sample (grey) versus distance up to $D = 100$ Mpc. Squares indicate the CT AGN in our sample that are detected in the *Swift*-BAT survey. The dashed line divides the high/low luminosity AGN. *Swift*-BAT AGN within 15 Mpc that are not in our sample are discussed in Section 2.1.

III] line (see Fig. 9 of GA09). Therefore, in addition to the two widely used CT AGN selection criteria described in previous sections, we also explore the use of the [Ne V] line as an intrinsic AGN luminosity indicator and a tool to identify CT candidates.

We compared the observed 2–10 keV and [Ne V] luminosities for our sample with the intrinsic correlation found by Bierschenk et al. (2024), which was derived using the *Swift*-BAT AGN sample. Again, we classified those AGN with observed 2–10 keV luminosities lying more than 25× below this intrinsic relationship provided by Bierschenk et al. (2024) as likely to be CT. This is shown in Fig. 11 (right). This technique managed to identify four out of six (67^{+33}_{-43} per cent) of our confirmed CT AGN. The two CT AGN that were missed are NGC 4945 and NGC 5194. In fact, their observed X-ray luminosities are well in agreement with the intrinsic relationship, indicating that they would have been considered as unobscured if we were relying on this technique to estimate the AGN obscuration. Nevertheless, none of our Compton-thin/unobscured AGN are selected as CT using this method, including those with $L_{2-10,int} < 10^{40}$ erg s^{-1}, with the exception of NGC 660. In fact for these sources, their luminosities are consistent with the established relationship, which could be used as evidence to support that the [Ne V] emission detected by GA09 in this galaxies genuinely originate from AGN activities instead of other processes. Adopting the CT solution for NGC 660 would give an intrinsic 2–10 keV luminosity that is consistent with the established X-ray-[Ne V] relationship, supporting this scenario.

6 COMPTON-THICK AGN FRACTION AND N_H DISTRIBUTION

Based on our results presented in Table 3, we find that the majority of our sources; i.e. 14/19 (74^{+26}_{-29} per cent) are obscured, and 6/19 (i.e. 32^{+30}_{-18} per cent) are CT (37^{+33}_{-20} per cent if including NGC 660; see Annuar et al. 2020). The CT AGN fraction is significantly higher than that directly observed in the entire *Swift*-BAT sample (i.e. $7.6^{+1.1}_{-2.1}$ per cent over the entire X-ray luminosity range of the *Swift*-BAT AGN sample; log $L_{14-195} = 40$–46 erg s^{-1}; Ricci et al. 2015), even after accounting for the uncertainties due to small-number statistics for our sample. Their inferred intrinsic fraction however (i.e. 27 ± 4 per cent), is well in agreement with our value. Although the overall observed CT AGN fraction found for the *Swift*-BAT sample is significantly lower than the intrinsic fraction inferred, and also determined using our sample, Ricci et al. (2015) show that this discrepancy is due to a bias against finding relatively faint CT AGN at larger distances. This is demonstrated in Fig. 12 (top). From this figure, we can see that at a smaller distance of 20 Mpc, Ricci et al. (2015) found that the CT AGN population in the *Swift*-BAT sample is consistent with their inferred intrinsic fraction. Their CT fraction at $D \leq 20$ Mpc is also in agreement with our fraction at $D \leq 15$ Mpc. However, with our sample, we managed to identify additional lower luminosity CT AGN; i.e. NGC 1448 (Annuar et al. 2017) and possibly NGC 660 (Annuar et al. 2020; see Fig. 12 – bottom).[6]

The same conclusion can be made when comparing our results with *NuSTAR* study of the *Swift*-BAT sample by Torres-Albà et al. (2021) which only directly measured a CT fraction of ~ 8 per cent. However, when limiting down the sample to smaller redshift of $z \lesssim 0.01$, this fraction increases to 20 ± 5 per cent, consistent with our findings. In addition, our fraction is also well in agreement with that directly found by the *NuSTAR* study of mid-IR (NuLANDS; Boorman et al. 2024a) and optical AGN (Kammoun et al. 2020), which measure CT fractions of ~ 35 per cent and ∼37–53 per cent, respectively.

This consistency also holds when we compare our results with the CT AGN X-ray luminosity functions (XLFs) from previous studies, which estimate CT AGN fractions ranging from ∼17–24 per cent (e.g. Akylas et al. 2016; Ananna et al. 2022; Laloux et al. 2023; Georgantopoulos et al. 2025), in agreement with our findings. The lower luminosity limit in these studies is typically log $L_X = 41$ erg s^{-1}. Laloux et al. (2023) extended down to $L_X = 40$ erg s^{-1}; however, the local CT XLF in that study remains an upper limit. In contrast, our work provides direct observational constraints down to this low luminosity limit.

Akylas et al. (2024) did a similar study to ours using a sample of infrared-selected AGN within 100 Mpc, but focusing on luminous

[6]The 2–10 keV intrinsic luminosities for the *Swift*-BAT AGN were converted from their 14–195 keV luminosities using the scaling relation from Rigby et al. (2009).

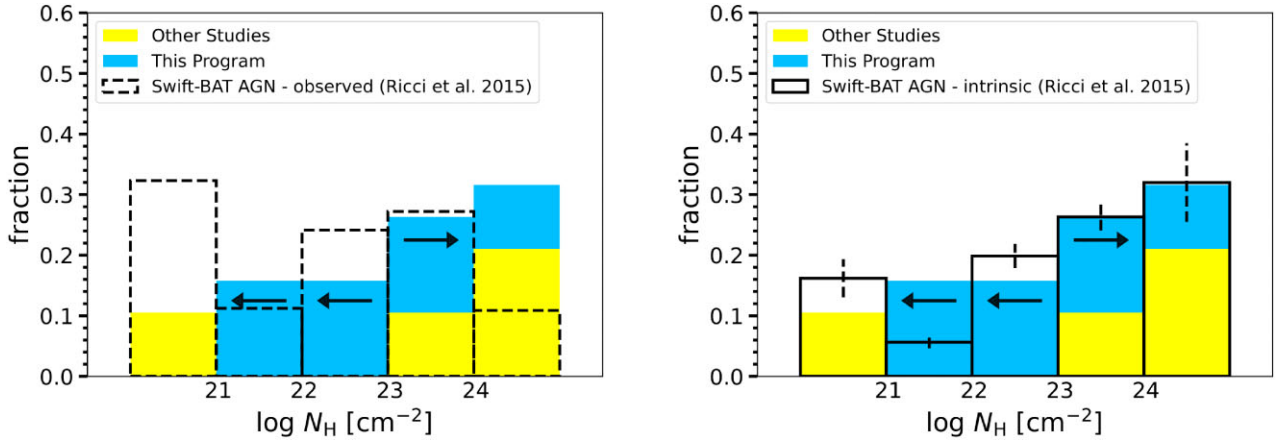

Figure 13. The N_H distribution for our sample compared to the observed (left) and intrinsic (right) N_H distributions of the *Swift*-BAT AGN sample with $\log L_{14-195} = 40.0$–43.7 erg s^{-1} (Ricci et al. 2015). Yellow indicates those with N_H measurements from other studies, whilst blue indicates those that were measured as part of this programme (Annuar et al. 2015; Annuar et al. 2017; Annuar et al. 2020; this work).

AGN with $\log L_{12\mu m} > 42.3$ erg s^{-1}. They found a CT fraction of 25 ± 5 per cent, which is consistent with our overall fraction. This is also in agreement with our CT AGN fraction below this 12μm luminosity threshold; i.e. 19^{+30}_{-14} per cent (3/16). However, above this threshold ($\log L_{12\,\mu m} > 42.3$ erg s^{-1}), we obtained a 100^{+0}_{-73} per cent (3/3) CT population, which is much higher than that found by Akylas et al. (2024). Nevertheless, within the large statistical uncertainty of our value, they agree with each other. We also found the same results when considering a similar 2–10 keV X-ray luminosity threshold of $L_{2-10,int} = 10^{42}$ erg s^{-1}, where we found a CT AGN fraction of 19^{+30}_{-14} per cent (3/16) below this limit. This indicates a moderate CT AGN population within this low-luminosity regime, consistent with those found at higher luminosities.

Fig. 13 shows the N_H distribution of our AGN sample compared to the observed and intrinsic N_H distributions of the *Swift*-BAT AGN with comparable X-ray luminosities to our sample (i.e. $\log L_{14-195} = 40.0$–43.7 erg s^{-1}; Ricci et al. 2015). Based on this figure, the N_H distribution of the AGN in our sample seems to be different from the observed N_H distribution of the *Swift*-BAT AGN, particularly at the lowest and highest (CT) regimes. However, it agrees very well with the intrinsic N_H distribution inferred after taking into account the *Swift*-BAT survey sensitivity limit. This demonstrates that using our sample, we are able to directly identify a higher fraction of CT AGN as compared to that directly observed in the *Swift*-BAT survey, exemplifying the bias against finding CT AGN even in a hard X-ray survey such as *Swift*-BAT. Based on this figure, we can also see how much our program has significantly improved the knowledge of X-ray properties of the nearest AGN down to lower luminosity.

Based on Fig. 9, if we apply a luminosity cut-off of $L_{2-10,int} = 10^{40}$ erg s^{-1}, to separate low/high-luminosity AGN (Annuar et al. 2020) and also to match the lower luminosity end of the entire *Swift*-BAT AGN sample, the CT AGN fraction calculated for our sample above this luminosity is 50^{+49}_{-28} per cent (6/12). This is higher than that observed and predicted using the *Swift*-BAT sample. This demonstrates the large uncertainty in determining an accurate N_H distribution of the AGN population at this high-obscuration regime. We note that, however, the lower limit fraction calculated is consistent with the intrinsic fraction inferred by the *Swift*-BAT survey if we take into account the uncertainties due to small number statistics (i.e. 50^{+49}_{-28} per cent; see footnote 2).

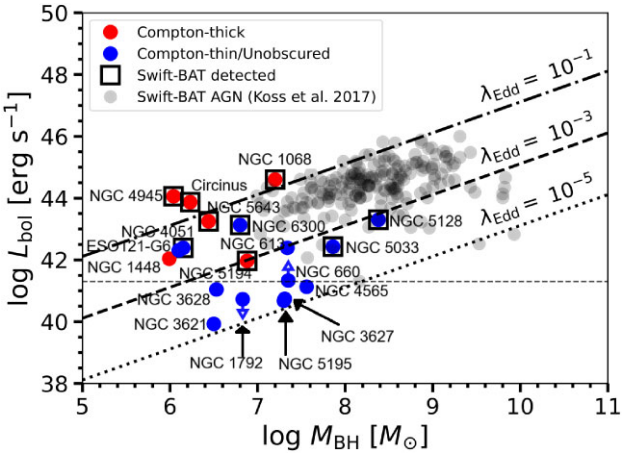

Figure 14. The bolometric luminosity versus M_{BH} for our sample and the *Swift*-BAT AGN sample (grey). Symbols are the same as in Fig. 11. The dashed and dotted lines indicate constant Eddington ratios of $\lambda_{Edd} = 10^{-5}$, 10^{-3}, and 10^{-1}, respectively. Figure adapted from Goulding et al. (2010).

7 DISCUSSION

7.1 Eddington ratio

In Fig. 14 we show a plot of the AGN bolometric luminosity, L_{bol}, as a function of black-hole mass, M_{BH}, for our sample and the *Swift*-BAT AGN sample (Koss et al. 2017). The bolometric luminosities for the AGN in our sample were calculated using their absorption-corrected 2–10 keV luminosities, assuming bolometric corrections of $\kappa \approx 20$ for those with $L_{2-10,int} \geq 10^{40}$ erg s^{-1} (e.g. Elvis et al. 1994; Vasudevan et al. 2010), and $\kappa \approx 13$ ($L_{2-10\ keV,\ int}/10^{41}$ erg s^{-1})$^{-0.37}$) for the lower luminosity AGN (Nemmen, Storchi-Bergmann & Eracleous 2014). The bolometric luminosities for the *Swift*-BAT AGN are given in Koss et al. (2017) and were determined from their 14–195 keV luminosities. Koss et al. (2017) measured M_{BH} for the *Swift*-BAT AGN sample using the velocity dispersion method, whilst for our AGN sample, the M_{BH} values were determined using a range of techniques (e.g. maser mapping, velocity dispersion, and bulge luminosity; see GA09 for more details).

The M_{BH} distribution of the two samples are significantly different from each other, with our sample dominating at lower M_{BH}. Per-

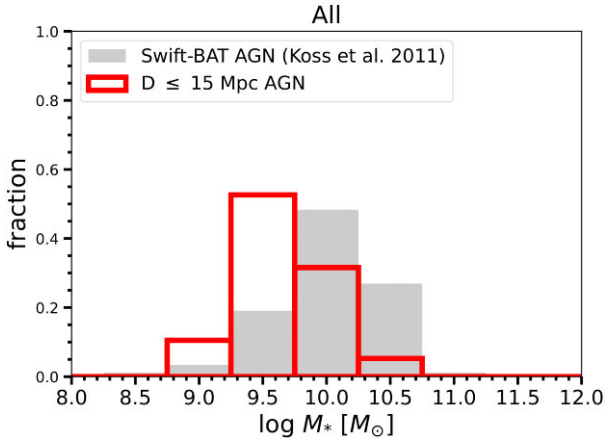

Figure 15. M_* distributions for our sample (red) and the *Swift*-BAT sample (grey).

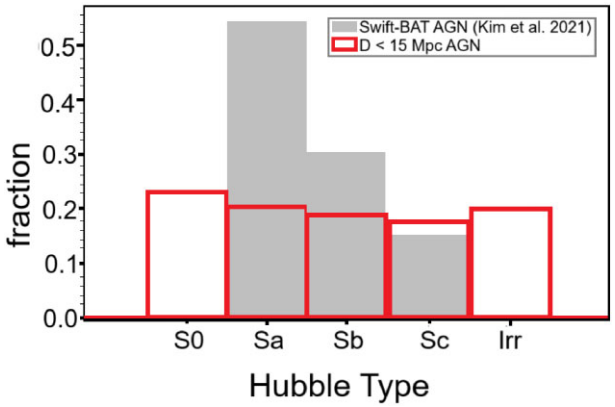

Figure 16. The distribution of Hubble type for our sample (red) and the *Swift-BAT* sample (grey; Kim et al. 2021).

forming a Kolmogorov–Smirnov (KS) test on the $M_{\rm BH}$ distributions between the two samples produced a KS test probability of $P_{\rm KS} \sim 2 \times 10^{-11}$, indicating that the two distributions are significantly different from each other. The mean $M_{\rm BH}$ calculated for our sample, $\log <M_{\rm BH,15Mpc}> = 6.88 \pm 0.65$ M$_\odot$, is ≈ 1.5 dex lower than that determined for the *Swift*-BAT sample, $\log <M_{\rm BH,BAT}> = 8.32 \pm 0.61$ M$_\odot$.

Fig. 14 shows that our sample has AGN bolometric luminosities in the range of $L_{\rm bol} \sim 10^{39}$–10^{45} erg s^{-1}, extending to lower luminosities than the *Swift*-BAT sample. The Eddington-ratio ranges probed by both samples however are similar, although the latter dominates at higher accretion rates of $\lambda_{\rm Edd} \geq 10^{-3}$, and our sample is more evenly distributed between Eddington ratios below and above of this threshold. Interestingly, the majority of our sample at high Eddington ratios (i.e. $\lambda_{\rm Edd} \geq 10^{-3}$) are CT, whereas the majority of AGN at lower Eddington ratios ($\lambda_{\rm Edd} < 10^{-3}$) are unobscured or just mildly obscured. These results are consistent with that found by past studies (e.g. Ho 2008; Draper & Ballantyne 2010).

7.2 Host–galaxy properties

In this section we compare the host-galaxy and optical AGN properties of our sample with those of the *Swift*-BAT AGN sample to investigate any potential differences between the two samples, given the unique parameter space that we probe using our $D \leq 15$ Mpc AGN sample (i.e. lower AGN luminosities and black hole masses).

7.2.1 Stellar Mass

Firstly, we investigated the stellar mass (M_*) distributions for our sample and the *Swift*-BAT sample. We show the comparison between the two distributions in Fig. 15. The stellar masses for our sample were determined using the K-band magnitude and the $J-K$ colour from the 2MASS Large Galaxy Atlas (Jarrett et al. 2003). We calculated M_* for our sample using the relation derived by Westmeier, Braun & Koribalski (2011) between the K-band stellar mass-to-light ratio and the $J-K$ colour index. Meanwhile, M_* for the *Swift*-BAT sample was derived using spectral energy distribution fitting by Koss et al. (2011). For one of our AGN (NGC 4051) that has a measurement in Koss et al. (2011), we used the value given by that paper as we believe that it is more reliable. However, we note that the value that we calculated for the source using our method ($\log M_* = 9.60\,{\rm M}_\odot$) is in agreement with that derived by Koss et al. (2011) ($\log M_* = 9.44\,{\rm M}_\odot$), demonstrating the reliability of our method. Additionally, NGC 4051 is a broad-line AGN, where the AGN contribution could significantly affect the optical-near-IR emission. This makes it a challenging case, and it is reassuring that our method provides a consistent stellar mass with that derived by Koss et al. (2011).

Fig. 15 shows that the galaxies in our sample generally have lower stellar masses as compared to the *Swift*-BAT sample. The mean stellar mass measured for our sample, $\log <M_{*,\rm 15Mpc}> = 9.93 \pm 0.31$ M$_\odot$, is ~ 0.3 dex lower than that calculated for the *Swift*-BAT sample; i.e. $\log <M_{*,\rm BAT}> = 10.24 \pm 0.44$ $M_\odot$. This can be attributed to the smaller $M_{\rm BH}$ and volume that we probe in our sample as compared to the *Swift*-BAT survey. Within the statistical uncertainties however, the stellar masses for the two samples are in agreement with each other. We performed a KS test between the two distributions and found that they are not significantly different from each other, with $P_{\rm KS} \sim 0.9$.

Comparing the $M_{\rm BH}$ (see Section 7.1) with the M_* distributions, we can see a more significant difference in $M_{\rm BH}$ between the two samples as compared to M_*. A reason for this could be due to the *Swift*-BAT sample having more bulge-dominated systems as compared to our sample (see Fig. 16). In these systems, the $M_{\rm BH}$ and M_* ratio ($M_{\rm BH}/M_*$) is higher than for weak/bulgeless systems (e.g. Reines & Volonteri 2015), which is the case for most of our sources.

7.2.2 Star formation rate

We also compare the star formation rate (SFR) distributions between our sample and the *Swift*-BAT sample. The two distributions are shown in Fig. 17. We calculated the SFR for our sample using the far-IR luminosity from IRAS (Sanders et al. 2003) following Murphy et al. (2011). For the *Swift*-BAT sample, Shimizu et al. (2017) determined the SFR of the AGN using the SF luminosity obtained through spectral energy distribution decomposition, and then using the same $L_{\rm IR}$-SFR conversion from Murphy et al. (2011) as our study. For overlapping sources in both samples (i.e. NGC 5033 and NGC 6300), we used the measurements from Shimizu et al. (2017) as we believe that the technique is more reliable. We note that, the values calculated from our method for the two sources are comparable (agree within ~0.3 dex) to those derived from Shimizu et al. (2017) measurements. In both cases, our values are systematically lower than those determined by Shimizu et al. (2017). For NGC 6300, the difference is smaller (~0.1 dex), while for NGC 5033, our value

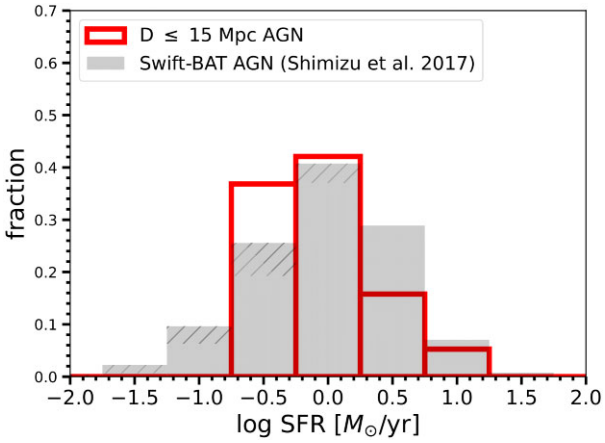

Figure 17. SFR distributions for our sample (red) and the *Swift*-BAT sample to their (grey). Grey hatch indicates the *Swift*-BAT AGN which have upper limits SFRs.

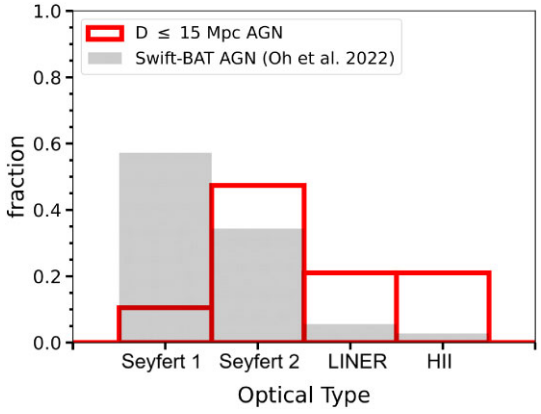

Figure 18. The distribution of optical nuclear classifications for our sample (red) and the *Swift*-BAT sample (grey).

is ∼0.3 dex lower. However, these differences do not significantly affect our results or the overall SFR distributions.

Overall, we found that the median SFR for our sample, log $<\mathrm{SFR}>_{15\mathrm{Mpc}} = 0.25 \pm 0.39$ $\mathrm{M}_\odot$ yr^{-1} is consistent with that found for the *Swift*-BAT AGN sample within the statistical uncertainties; i.e. log $<\mathrm{SFR}>_{\mathrm{BAT}} = 0.23^{+0.58}_{-0.80}$ $\mathrm{M}_\odot$ yr^{-1} (Shimizu et al. 2017). Performing a KS test on the SFR distributions between the two samples provide a KS test probability of $P_{\mathrm{KS}} \sim 0.9$ and 0.8 when excluding and including sources with upper limit SFR in the *Swift*-BAT sample, respectively. This indicates that the two distributions are not significantly different from each other. These results indicate that the galaxies in our sample have similar SFR to the *Swift*-BAT sample, despite the lower M_{BH} and M_* probed in our sample. However, we caution that this may be attributed to the IR luminosity cut-off applied by GA09 of $L_{\mathrm{IR}} = 3 \times 10^9$ $\mathrm{L}_\odot$ (corresponding to log SFR $= -0.49$ $\mathrm{M}_\odot$ yr^{-1}, assuming that all of the IR luminosity is due to star formation), to select the AGN sample which could bias the sample against selecting $D \leq 15$ Mpc AGN with low SFRs.

7.2.3 *Optical type*

Finally, we compare the distribution of the optical classifications of the AGN in our sample with that of the *Swift*-BAT AGN sample (Oh et al. 2022). This is shown in Fig. 18. This diagram shows that most of our AGN are classified as Seyfert 2s. We have significantly more LINERs and HII galaxies, but a lower fraction of Seyfert 1s than *Swift*-BAT. The higher fractions of LINER and HII galaxies found in our sample show that we managed to identify relatively weaker AGN that are not identified in the optical. The *Swift*-BAT survey is limited by its sensitivity ($f_{14-195} \sim 10^{-11}$ erg s^{-1} cm^{-2}), and is therefore also biased against finding weak AGN. This may be the reason why our sample has a lower fraction of Seyfert 1s; i.e. due to the challenge in identifying the broad line components in the optical spectra of weak AGN since they generally have lower black hole masses, and the optical spectra can also be significantly contaminated by the host galaxies. It is also interesting to note that most of our HII nuclei (3/4, 75^{+25}_{-55} per cent) are heavily obscured AGN with $N_{\mathrm{H}} > 10^{23}$ cm^{-2}, suggesting that these nuclei suffer significant obscuration by both the host-galaxy and the AGN tori (see also GA09).

8 CONCLUSION

We present a census of the CT AGN population and the N_{H} distribution of AGN in our cosmic backyard using an AGN sample within $D = 15$ Mpc. We use N_{H} values measured directly from X-ray spectroscopic analysis using data from multiple observatories, mainly *Chandra* and *NuSTAR*. Our sample consists of AGN with intrinsic 2–10 keV luminosity in the range of $L_{2-10,\mathrm{int}} = 10^{37}$–$10^{43}$ erg s^{-1}, probing into a new parameter space that is not possible for more distant samples. Here is a summary of our main results:

(i) We found that 74^{+26}_{-29} per cent (14/19) of our sample is obscured AGN, with 32^{+30}_{-18} per cent (6/19) classified as Compton-thick (CT). This CT AGN fraction is significantly higher than that observed in the *Swift*-BAT survey but aligns with the fraction inferred after correcting for the survey's sensitivity limits. Our N_{H} distribution also agrees well with the corrected values. Applying a luminosity cut-off of $L_{2-10,\mathrm{int}} = 10^{40}$ erg s^{-1}, we find a CT AGN fraction of 50^{+49}_{-28} per cent (6/12) above this threshold. This is significantly higher than that observed by *Swift*-BAT, but fully consistent with the inferred value within the uncertainties. Overall, our results provide direct observational evidence for AGN that are predicted by the *Swift*-BAT survey but remain undetected due to the survey's flux limitations.

(ii) If we consider only the typically defined low-luminosity regime of $L_{2-10,\mathrm{int}} \leq 10^{42}$ erg s^{-1}, we determined a CT AGN fraction of 19^{+30}_{-14} per cent (3/16) within this relatively understudied domain. This is fully consistent with those observed at higher luminosities.

(iii) Overall, the multiwavelength data seem to support our X-ray analysis results, with the exception of a few cases, especially the intrinsically low-luminosity sources with $L_{2-10,\mathrm{int}} \sim 10^{40}$ erg s^{-1} in the X-ray:12 μm diagnostic diagram. These cases align with the typical limit of the intrinsic correlation derived. This suggests that such correlation may break down at lower AGN luminosities or that significant flux contamination from off-nuclear sources may affect these low-luminosity objects. Recent deactivation of the nuclear source, as well as extreme CT obscuration could also explain the discrepancies.

(iv) All of our sources with $L_{2-10,\mathrm{int}} < 10^{40}$ erg s^{-1} (with the exception of NGC 660) are either unobscured or only mildly obscured, with $N_{\mathrm{H}} \lesssim 10^{22}$ cm^{-2}. This suggests that at such low luminosities, the AGN torus may be underdeveloped or absent, supporting previous studies that have proposed this scenario.

(v) The Eddington-ratio range probed by our sample is similar to that of the *Swift*-BAT AGN sample, although the latter dominates at higher accretion rates. Majority of our sample at $\lambda_{\mathrm{Edd}} \geq 10^{-3}$ tend to be CT AGN, while AGN at $\lambda_{\mathrm{Edd}} < 10^{-3}$ are mainly unobscured or just

mildly obscured. On the other hand, our sample has lower black-hole masses, peaking at $\sim 10^6$ $M_\odot$, ~ 1.5 dex lower than the *Swift*-BAT sample, showing that our $D < 15$ Mpc sample predominantly selects low-mass AGN.

(vi) In terms of basic host-galaxy properties, our sample shows star formation rates that are comparable to those in the *Swift*-BAT sample. However, most AGN in our sample are hosted by galaxies with lower stellar masses. This could be attributed to the smaller black hole masses (M_{BH}) and the more-local volume we probe compared to the *Swift*-BAT survey. Additionally, our sample contains a significantly higher number of LINERs and HII-type optical nuclear spectra, which are largely missed by the *Swift*-BAT survey. This indicates that we have identified weaker AGN, or AGN that are heavily obscured by their host galaxies, causing them undetectable in optical wavelength.

Deeper observations with current facilities, or more sensitive and higher spatial resolution observations such as with the *JWST* mission, will be useful in constraining the 12μm and [Ne V] nuclear emission which are currently not complete and might be contaminated by non-AGN emission. A future high-energy X-ray mission with higher sensitivity than *NuSTAR* will also be crucial in further constraining the X-ray properties of the low-luminosity AGN, including NGC 660 which is likely to be CT, and pushing this study out to a larger volume. Additionally, monitoring observations would also be useful to investigate whether variability or source deactivation could be the contributing cause for the multiwavelength discrepancies in the low-luminosity sources, such as the case for ESO 121-G6 (Annuar et al. 2020) and NGC 3627 (Saade et al. 2022), respectively. These will not only allow us to improve the AGN N_H distribution within the local volume, but also investigate the properties of low-luminosity AGN and test current theories on these sources; e.g. whether they have different physical structure than their more luminous counterparts.

ACKNOWLEDGEMENTS

AA acknowledges financial support from *Universiti Kebangsaan Malaysia*'s *Geran Universiti Penyelidikan* grant code GUP-2023-033 and the Merdeka Award Grant for International Attachment 2021. DMA acknowledges the Science and Technology Facilities Council (STFC) for support through grant code ST/T000244/1. MNR acknowledges support from the MyBrainSc Scholarship programme under the Ministry of Higher Education Malaysia (MoHE). CR acknowledges support from Fondecyt Regular grant 1230345 and ANID BASAL project FB210003. DRB is supported in part by NASA award 80NSSC24K0212 and NSF grants AST-2307278 and AST-2407658.

DATA AVAILABILITY

This work made use of data from the *NuSTAR* mission. *NuSTAR* is a project led by the California Institute of Technology (Caltech), managed by the Jet Propulsion Laboratory (JPL), and funded by the National Aeronautics and Space Administration (NASA). We thank the *NuSTAR* Operations, Software and Calibrations teams for support with these observations. This research has made use of the *NuSTAR* Data Analysis Software (NUSTARDAS) jointly developed by the ASI Science Data Center (ASDC, Italy) and Caltech (USA). The scientific results reported in this article are based on observations made by the *Chandra X-ray Observatory* and data obtained from the Chandra Data Archive. This research has made use of software provided by the Chandra X-ray Center (CXC) in the application packages CIAO. This work was also based on observations obtained with *XMM-Newton*, an ESA science mission with instruments and contributions directly funded by ESA Member States and NASA.

This research made use of various Python packages. We also used data obtained through the High Energy Astrophysics Science Archive Research Center (HEASARC) Online Service, provided by the NASA/Goddard Space Flight Center. The data used in this paper are publicly available and can be accessed and downloaded from NASA's HEASARC (https://heasarc.gsfc.nasa.gov/docs/archive.html); details of the X-ray observations, including their identification numbers, are provided in Table 2. Most of the data presented in this research were taken from GA09 or Goulding et al. (2010), while the remaining data sources are specified in the notes section of Table 1. In addition, we used the NASA/IPAC Extragalactic Database (NED), which is operated by the Jet Propulsion Laboratory, California Institute of Technology, under contract with NASA.

Facilities: *Chandra*, *NuSTAR*, *Swift* and *XMM–Newton*.

REFERENCES

Aalto S. et al., 2019, A&A, 627, A147
Akylas A., Georgakakis A., Georgantopoulos I., Brightman M., Nandra K., 2012, A&A, 546, A98
Akylas A., Georgantopoulos I., Gandhi P., Boorman P., Greenwell C. L., 2024, A&A, 692, A250
Akylas A., Georgantopoulos I., Ranalli P., Gkiokas E., Corral A., Lanzuisi G., 2016, A&A, 594, A73
Alexander D. M., 2001, MNRAS, 320, L15
Ananna T. T. et al., 2019, ApJ, 871, 240
Ananna T. T. et al., 2022, ApJS, 261, 9
Annuar A. et al., 2015, ApJ, 815, 36
Annuar A. et al., 2017, ApJ, 836, 165
Annuar A. et al., 2020, MNRAS, 497, 229
Antonucci R., 1993, ARA&A, 31, 473
Arévalo P. et al., 2014, ApJ, 791, 81
Asmus D. et al., 2020, MNRAS, 494, 1784
Asmus D., Gandhi P., Hönig S. F., Smette A., Duschl W. J., 2015, MNRAS, 454, 766
Asmus D., Hönig S. F., Gandhi P., 2016, ApJ, 822, 109
Asmus D., Hönig S. F., Gandhi P., Smette A., Duschl W. J., 2014, MNRAS, 439, 1648
Assef R. J. et al., 2013, ApJ, 772, 26
Audibert A. et al., 2019, A&A, 632, A33
Baldwin J. A., Phillips M. M., Terlevich R., 1981, PASP, 93, 5
Baloković M. et al., 2014, ApJ, 794, 111
Baloković M. et al., 2018, ApJ, 854, 42
Barth A. J., Strigari L. E., Bentz M. C., Greene J. E., Ho L. C., 2009, ApJ, 690, 1031
Bassani L., Dadina M., Maiolino R., Salvati M., Risaliti G., Della Ceca R., Matt G., Zamorani G., 1999, ApJS, 121, 473
Bauer F. E. et al., 2015, ApJ, 812, 116
Baumgartner W. H., Tueller J., Markwardt C. B., Skinner G. K., Barthelmy S., Mushotzky R. F., Evans P. A., Gehrels N., 2013, ApJS, 207, 19
Bianchi S., Matt G., Fiore F., Fabian A. C., Iwasawa K., Nicastro F., 2002, A&A, 396, 793
Bierschenk M. et al., 2024, ApJ, 976, 257
Boorman P. G. et al., 2024a, ApJ, 978, 118
Boorman P. et al., 2024b, American Astronomical Society Meeting Abstracts, 175.02
Brandt W. N., Alexander D. M., 2015, A&AR, 23, 1
Brightman M., Nandra K., 2008, MNRAS, 390, 1241
Brightman M., Nandra K., 2011, MNRAS, 414, 3084
Burlon D., Ajello M., Greiner J., Comastri A., Merloni A., Gehrels N., 2011, ApJ, 728, 58
Cappi M. et al., 2006, A&A, 446, 459
Cash W., 1979, ApJ, 228, 939

Castangia P., Panessa F., Henkel C., Kadler M., Tarchi A., 2013, MNRAS, 436, 3388
Chiaberge M., Gilli R., Macchetto F. D., Sparks W. B., 2006, ApJ, 651, 728
Cisternas M. et al., 2013, ApJ, 776, 50
Comastri A., Gilli R., Marconi A., Risaliti G., Salvati M., 2015, A&A, 574, L10
da Silva P., Menezes R. B., Steiner J. E., 2020a, MNRAS, 492, 5121
da Silva P., Menezes R. B., Steiner J. E., Fraga L., 2020b, MNRAS, 496, 943
Diamond-Stanic A. M., Rieke G. H., Rigby J. R., 2009, ApJ, 698, 623
Diaz Y. et al., 2023, A&A, 669, A114
Done C., Madejski G. M., Życki P. T., Greenhill L. J., 2003, ApJ, 588, 763
Draper A. R., Ballantyne D. R., 2010, ApJ, 715, L99
Dudik R. P., Satyapal S., Gliozzi M., Sambruna R. M., 2005, ApJ, 620, 113
Elitzur M., Ho L. C., 2009, ApJ, 701, L91
Elitzur M., Shlosman I., 2006, ApJ, 648, L101
Elvis M. et al., 1994, ApJS, 95, 1
Esparza-Arredondo D., Osorio-Clavijo N., González-Martín O., Victoria-Ceballos C., Haro-Corzo S. A. R., Reyes-Amador O. U., López-Sánchez J., Pasetto A., 2020, ApJ, 905, 29
Falcón-Barroso J., Ramos Almeida C., Böker T., Schinnerer E., Knapen J. H., Lançon A., Ryder S., 2014, MNRAS, 438, 329
Feruglio C., Maiolino R., Piconcelli E., Menci N., Aussel H., Lamastra A., Fiore F., 2010, A&A, 518, L155
Filho M. E., Barthel P. D., Ho L. C., 2000, ApJS, 129, 93
Fruscione A. et al., 2006, in Silva D. R., Doxsey R.E., eds, Proc. SPIE Conf. Ser. Vol. 6270, Observatory Operations: Strategies, Processes, and Systems. SPIE, Bellingham, p. 62701V
Fürst F. et al., 2016, ApJ, 819, 150
Gandhi P., Horst H., Smette A., Hönig S., Comastri A., Gilli R., Vignali C., Duschl W., 2009, A&A, 502, 457
Gehrels N., 1986, ApJ, 303, 336
Georgantopoulos I., Pouliasis E., Ruiz A., Akylas A., 2025, A&A, 695, A128
Gilli R., Comastri A., Hasinger G., 2007, A&A, 463, 79
Gliozzi M., Satyapal S., Eracleous M., Titarchuk L., Cheung C. C., 2009, ApJ, 700, 1759
González-Alfonso E., Sakamoto K., 2019, ApJ, 882, 153
González-Martín O. et al., 2017, ApJ, 841, 37
González-Martín O., Masegosa J., Márquez I., Guainazzi M., Jiménez-Bailón E., 2009, A&A, 506, 1107
Goulding A. D., Alexander D. M., 2009, MNRAS, 398, 1165
Goulding A. D., Alexander D. M., Lehmer B. D., Mullaney J. R., 2010, MNRAS, 406, 597
Goulding A. D., Alexander D. M., Mullaney J. R., Gelbord J. M., Hickox R. C., Ward M., Watson M. G., 2011, MNRAS, 411, 1231
Greenhill L. J., Kondratko P. T., Lovell J. E. J., Kuiper T. B. H., Moran J. M., Jauncey D. L., Baines G. P., 2003, ApJ, 582, L11
Harrison F. A. et al., 2013, ApJ, 770, 103
Helou G., Walker D. W., eds, 1988, Infrared astronomical satellite (IRAS) catalogs and atlases. Volume 7: The small scale structure catalog , NASA RP-1190,Vol. 7
Hickox R. C., Alexander D. M., 2018, ARA&A, 56, 625
Ho L. C., 2008, ARA&A, 46, 475
Ho L. C., Filippenko A. V., Sargent W. L. W., 1997, ApJS, 112, 315
Hönig S. F., 2019, ApJ, 884, 171
Hönig S. F., Beckert T., 2007, MNRAS, 380, 1172
Hopkins P. F., Hernquist L., Cox T. J., Kereš D., 2008, ApJS, 175, 356
Horst H., Gandhi P., Smette A., Duschl W. J., 2008, A&A, 479, 389
Houck J. R. et al., 2004, ApJS, 154, 18
Hummel E., Jorsater S., 1992, A&A, 261, 85
Hummel E., Jorsater S., Lindblad P. O., Sandqvist A., 1987, A&A, 172, 51
Ishibashi W., Fabian A. C., 2016, MNRAS, 463, 1291
Iwasawa K. et al., 2011, A&A, 528, A137
Iwasawa K., Fabian A. C., Matt G., 1997, MNRAS, 289, 443
Jana A., Chatterjee A., Kumari N., Nandi P., Naik S., Patra D., 2020, MNRAS, 499, 5396
Jarrett T. H., Chester T., Cutri R., Schneider S. E., Huchra J. P., 2003, AJ, 125, 525
Kalberla P. M. W., Burton W. B., Hartmann D., Arnal E. M., Bajaja E., Morras R., Pöppel W. G. L., 2005, A&A, 440, 775
Kammoun E. S. et al., 2020, ApJ, 901, 161
Kauffmann G. et al., 2003, MNRAS, 346, 1055
Kewley L. J., Dopita M. A., Sutherland R. S., Heisler C. A., Trevena J., 2001, ApJ, 556, 121
Kim M., Barth A. J., Ho L. C., Son S., 2021, ApJS, 256, 40
Kirkpatrick A. et al., 2013, ApJ, 763, 123
Kocevski D. D. et al., 2015, ApJ, 814, 104
Kondratko P. T. et al., 2006, ApJ, 638, 100
Koss M. et al., 2017, ApJ, 850, 74
Koss M., Mushotzky R., Veilleux S., Winter L. M., Baumgartner W., Tueller J., Gehrels N., Valencic L., 2011, ApJ, 739, 57
Laloux B. et al., 2023, MNRAS, 518, 2546
Lansbury G. B. et al., 2014, ApJ, 785, 17
Leitherer C., Byler N., Lee J. C., Levesque E. M., 2018, ApJ, 865, 55
Li A., Draine B. T., 2001, ApJ, 554, 778
Luo B. et al., 2013, ApJ, 772, 153
Madejski G., Życki P., Done C., Valinia A., Blanco P., Rothschild R., Turek B., 2000, ApJ, 535, L87
Madsen K. K. et al., 2015, ApJS, 220, 8
Magdziarz P., Zdziarski A. A., 1995, MNRAS, 273, 837
Maoz D., Nagar N. M., Falcke H., Wilson A. S., 2005, ApJ, 625, 699
Marchesi S. et al., 2019, ApJ, 872, 8
Marinucci A., Risaliti G., Wang J., Nardini E., Elvis M., Fabbiano G., Bianchi S., Matt G., 2012, MNRAS, 423, L6
Martín S. et al., 2016, A&A, 590, A25
Martínez-Sansigre A., Rawlings S., Lacy M., Fadda D., Marleau F. R., Simpson C., Willott C. J., Jarvis M. J., 2005, Nature, 436, 666
Mason R. E. et al., 2012, AJ, 144, 11
Matt G. et al., 1997, A&A, 325, L13
Matt G., Fabian A. C., Guainazzi M., Iwasawa K., Bassani L., Malaguti G., 2000, MNRAS, 318, 173
McKernan B., Ford K. E. S., Reynolds C. S., 2010, MNRAS, 407, 2399
Miyamoto Y., Nakai N., Seta M., Salak D., Nagai M., Kaneko H., 2017, PASJ, 69, 83
Moorwood A. F. M., Glass I. S., 1984, A&A, 135, 281
Mould J. R. et al., 2000, ApJ, 529, 786
Murphy E. J. et al., 2011, ApJ, 737, 67
Murphy E. J. et al., 2012, ApJ, 761, 97
Nagar N. M., Falcke H., Wilson A. S., 2005, A&A, 435, 521
Nandra K., O'Neill P. M., George I. M., Reeves J. N., 2007, MNRAS, 382, 194
Negus J., Comerford J. M., Sánchez F. M., Revalski M., Riffel R. A., Bundy K., Nevin R., Rembold S. B., 2023, ApJ, 945, 127
Nemmen R. S., Storchi-Bergmann T., Eracleous M., 2014, MNRAS, 438, 2804
Oh K. et al., 2018, ApJS, 235, 4
Oh K. et al., 2022, ApJS, 261, 4
Osorio-Clavijo N., González-Martín O., Sánchez S. F., Esparza-Arredondo D., Masegosa J., Victoria-Ceballos C., Hernández-García L., Díaz Y., 2022, MNRAS, 510, 5102
Panessa F., Bassani L., Cappi M., Dadina M., Barcons X., Carrera F. J., Ho L. C., Iwasawa K., 2006, A&A, 455, 173
Pereira-Santaella M., Diamond-Stanic A. M., Alonso-Herrero A., Rieke G. H., 2010, ApJ, 725, 2270
Puccetti S. et al., 2014, ApJ, 793, 26
Reines A. E., Volonteri M., 2015, ApJ, 813, 82
Ricci C. et al., 2017a, ApJS, 233, 17
Ricci C. et al., 2017b, MNRAS, 468, 1273
Ricci C., Ueda Y., Koss M. J., Trakhtenbrot B., Bauer F. E., Gandhi P., 2015, ApJ, 815, L13
Rieke G. H., Lebofsky M. J., 1985, ApJ, 288, 618
Rigby J. R., Diamond-Stanic A. M., Aniano G., 2009, ApJ, 700, 1878
Risaliti G., Maiolino R., Salvati M., 1999, ApJ, 522, 157
Roche P. F., Aitken D. K., Smith C. H., James S. D., 1986, MNRAS, 218, 19P
Rovilos E. et al., 2014, MNRAS, 438, 494

Saade M. L., Brightman M., Stern D., Malkan M. A., García J. A., 2022, ApJ, 936, 162
Sakamoto K., Aalto S., Costagliola F., Martín S., Ohyama Y., Wiedner M. C., Wilner D. J., 2013, ApJ, 764, 42
Sakamoto K., González-Alfonso E., Martín S., Wilner D. J., Aalto S., Evans A. S., Harada N., 2021, ApJ, 923, 206
Sanders D. B., Mazzarella J. M., Kim D.-C., Surace J. A., Soifer B. T., 2003, AJ, 126, 1607
Sanders D. B., Mirabel I. F., 1996, ARA&A, 34, 749
Satyapal S., Vega D., Heckman T., O'Halloran B., Dudik R., 2007, ApJ, 663, L9
Schaerer D., Stasińska G., 1999, A&A, 345, L17
Setti G., Woltjer L., 1989, A&A, 224, L21
Shi Y., Rieke G. H., Ogle P. M., Su K. Y. L., Balog Z., 2014, ApJS, 214, 23
Shimizu T. T., Mushotzky R. F., Meléndez M., Koss M. J., Barger A. J., Cowie L. L., 2017, MNRAS, 466, 3161
Spoon H. W. W. et al., 2022, ApJS, 259, 37
Spoon H. W. W., Keane J. V., Tielens A. G. G. M., Lutz D., Moorwood A. F. M., 2001, A&A, 365, L353
Spoon H. W. W., Marshall J. A., Houck J. R., Elitzur M., Hao L., Armus L., Brandl B. R., Charmandaris V., 2007, ApJ, 654, L49
Stern D. et al., 2014, ApJ, 794, 102
Stierwalt S. et al., 2013, ApJS, 206, 1
Tombesi F., Meléndez M., Veilleux S., Reeves J. N., González-Alfonso E., Reynolds C. S., 2015, Nature, 519, 436
Torres-Albà N. et al., 2021, ApJ, 922, 252
Treister E., Urry C. M., 2012, Adv. Astron., 2012, 516193
Treister E., Urry C. M., Schawinski K., Cardamone C. N., Sanders D. B., 2010, ApJ, 722, L238
Treister E., Urry C. M., Virani S., 2009, ApJ, 696, 110
Turner T. J., Miller L., Reeves J. N., Braito V., 2017, MNRAS, 467, 3924
Ueda Y., Akiyama M., Hasinger G., Miyaji T., Watson M. G., 2014, ApJ, 786, 104
Urry C. M., Padovani P., 1995, PASP, 107, 803
Vasudevan R. V., Fabian A. C., Gandhi P., Winter L. M., Mushotzky R. F., 2010, MNRAS, 402, 1081
Véron-Cetty M. P., Véron P., 2006, A&A, 455, 773
Veron-Cetty M.-P., Veron P., 1986, A&AS, 66, 335
Weaver K. A. et al., 2010, ApJ, 716, 1151
Weedman D. W. et al., 2005, ApJ, 633, 706
Werner M. W. et al., 2004, ApJS, 154, 1
Westmeier T., Braun R., Koribalski B. S., 2011, MNRAS, 410, 2217
Wethers C. F. et al., 2024, A&A, 683, A27
Wright E. L. et al., 2010, AJ, 140, 1868
Wu H., Xue S. J., Xia X. Y., Deng Z. G., Mao S., 2002, ApJ, 576, 738
Xu W., Liu Z., Gou L., Liu J., 2016, MNRAS, 455, L26
Yaqoob T., 2012, MNRAS, 423, 3360

[1]*Department of Applied Physics, Faculty of Science and Technology, Universiti Kebangsaan Malaysia, 43600 UKM Bangi, Selangor, Malaysia*
[2]*Centre for Extragalactic Astronomy, Department of Physics, Durham University, South Road, Durham DH1 3LE, UK*
[3]*School of Physics and Astronomy, University of Southampton, Southampton SO17 1BJ, UK*
[4]*European Southern Observatory, Karl-Schwarzschild str. 2, D-85748 Garching bei Munchen, Germany*
[5]*Jet Propulsion Laboratory, California Institute of Technology, Pasadena, CA 91109, USA*
[6]*Gymnasium Schwarzenbek, D-21493 Schwarzenbek, Germany*
[7]*Center for Relativistic Astrophysics, School of Physics, Georgia Institute of Technology, 837 State Street, Atlanta, GA 30332-0430, USA*
[8]*Yale Center for Astronomy & Astrophysics, 52 Hillhouse Avenue, New Haven, CT 06511, USA*
[9]*Department of Physics, Yale University, P.O. Box 2018120, New Haven, CT 06520, USA*
[10]*Instituto de Astrofísica and Centro de Astroingeniería, Facultad de Física, Pontificia Universidad Católica de Chile, Casilla 306, Santiago 22, Chile*
[11]*Millennium Institute of Astrophysics (MAS), Nuncio Monseñor Sótero Sanz 100, Providencia, 7500011 Santiago, Chile*
[12]*Space Science Institute, 4750 Walnut Street, Suite 205, Boulder, CO 80301, USA*
[13]*Cahill Center for Astrophysics, California Institute of Technology, 1216 East California Boulevard, Pasadena, CA 91125, USA*
[14]*Department of Astronomy and Astrophysics, 525 Davey Lab, The Pennsylvania State University, University Park, PA 16802, USA*
[15]*Institute for Gravitation and the Cosmos, The Pennsylvania State University, University Park, PA 16802, USA*
[16]*Department of Physics, 104 Davey Laboratory, The Pennsylvania State University, University Park, PA 16802, USA*
[17]*Science and Technology Institute, Universities Space Research Association, Huntsville, AL 35805, USA*
[18]*Astrophysics Office, NASA Marshall Space Flight Center, ST12, Huntsville, AL 35812, USA*
[19]*German Aerospace Center (DLR), Space Operation and Astronaut Training, Oberpfaffenhofen, D-82234 Weßling, Germany*
[20]*Institute for Astronomy, University of Hawai'i, 2680 Woodlawn Dr, Honolulu, HI 96822, USA*
[21]*Department of Physics and Astronomy, University of Hawai'i at Mānoa, 2505 Correa Rd., Honolulu, HI 96822, USA*
[22]*Eureka Scientific, 2452 Delmer Street Suite 100, Oakland, CA 94602-3017, USA*
[23]*Department of Physics, The College of New Jersey, 2000 Pennington Road, Ewing, NJ 08628, USA*
[24]*Dipartimento di Fisica e Astronomia (DIFA), Università di Bologna, via Gobetti 93/2, I-40129 Bologna, Italy*
[25]*Department of Physics and Astronomy, Clemson University, Kinard Lab of Physics, Clemson, SC 29634-0978, USA*
[26]*INAF – Osservatorio di Astrofisica e Scienza dello Spazio di Bologna, Via Piero Gobetti, 93/3, I-40129 Bologna, Italy*
[27]*INAF - Osservatorio Astrofisico di Arcetri, Largo E. Fermi 5, 50125 Firenze, Italy*
[28]*Instituto de Estudios Astrofísicos, Facultad de Ingeniería y Ciencias, Universidad Diego Portales, Av. Ejército Libertador 441, 8370191 Santiago, Chile*
[29]*Kavli Institute for Astronomy and Astrophysics, Peking University, Beijing 100871, People's Republic of China*
[30]*INAF – Osservatorio Astronomico di Roma, Via di Frascati 33, I-00078 Monte Porzio Catone, Italy*

This paper has been typeset from a TEX/LATEX file prepared by the author.